Redox-sensitive E2 Rad6 controls cellular response to oxidative stress via K63-linked ubiquitination of ribosomes

Vanessa Simões[1],

Blanche K. Cizubu[1,5],

Lana Harley[1,5],

Ye Zhou[2],

Joshua Pajak[3],

Nathan A. Snyder[1],

Jonathan Bouvette[4],

Mario J. Borgnia[4],

Gaurav Arya[3],

Alberto Bartesaghi[2],

Gustavo M. Silva[1,6,*]

[1]Department of Biology, Duke University, Durham, NC 27708, USA

[2]Department of Computer Science, Department of Biochemistry, and Department of Electrical and Computer Engineering, Duke University, Durham, NC 27708, USA

[3]Department of Mechanical Engineering and Materials Science, Duke University, Durham, NC 27708, USA

[4]Genome Integrity and Structural Biology Laboratory, National Institute of Environmental Health Sciences, National Institutes of Health, Department of Health and Human Services, Durham, NC 27709, USA

[5]These authors contributed equally

[6]Lead contact

SUMMARY

*Correspondence: gustavo.silva@duke.edu.

Protein ubiquitination is an essential process that rapidly regulates protein synthesis, function, and fate in dynamic environments. Within its non-proteolytic functions, we showed that K63-linked polyubiquitinated conjugates heavily accumulate in yeast cells exposed to oxidative stress, stalling ribosomes at elongation. K63-ubiquitinated conjugates accumulate mostly because of redox inhibition of the deubiquitinating enzyme Ubp2; however, the role and regulation of ubiquitin-conjugating enzymes (E2) in this pathway remained unclear. Here, we show that the E2 Rad6 associates and modifies ribosomes during stress. We further demonstrate that Rad6 and its human homolog UBE2A are redox regulated by forming a reversible disulfide with the E1 ubiquitin-activating enzyme (Uba1). This redox regulation is part of a negative feedback regulation, which controls the levels of K63 ubiquitination under stress. Finally, we show that Rad6 activity is necessary to regulate translation, antioxidant defense, and adaptation to stress, thus providing an additional physiological role for this multifunctional enzyme.

Graphical abstract
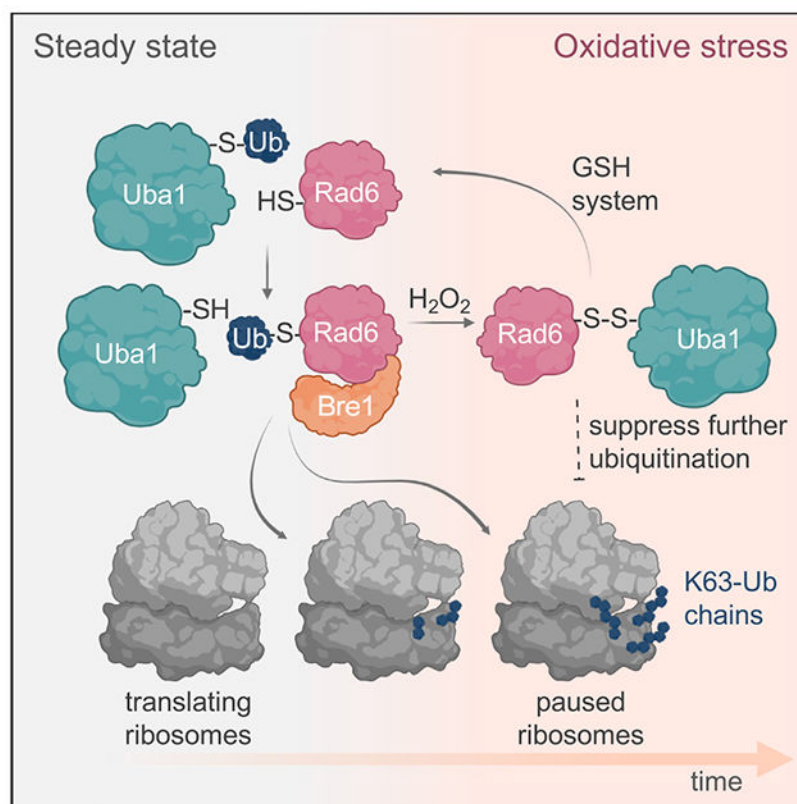
In brief

Cellular adaptation to oxidative stress requires refined control of gene expression at the translational level. Simões et al. reveal mechanistic aspects of how the ubiquitin-conjugating enzyme Rad6 is redox regulated and determines the levels of K63-linked ubiquitination of ribosomes to control the reprogramming of protein synthesis under stress.

INTRODUCTION

Translation is a highly regulated process in eukaryotes, controlled at multiple steps during cellular exposure to stress (Grant, 2011; Holcik and Sonenberg, 2005). Using mass spectrometry and cryoelectron microscopy (cryo-EM), our group recently showed that oxidative stress induces high levels of K63-linked polyubiquitin chains on ribosomes, which impact the elongation step of translation (Back et al., 2018; Silva et al., 2015; Zhou et al., 2020a). We named this pathway RTU for redox control of translation by ubiquitin (Dougherty et al., 2020). Protein ubiquitination is a multistep enzymatic process, and much remains unknown about the regulation of K63-linked ubiquitination of ribosomes in the RTU. In general, protein ubiquitination is achieved by the activity of ubiquitin conjugases (E2s) and ligases (E3s), which can be counteracted by deubiquitinases (DUBs) and degradation processes (Finley et al., 2012). In response to stress, a number of proteins are modified with K48-linked ubiquitin chains (Manohar et al., 2019), which are destined to proteasomal degradation, thus contributing to the control of protein abundance (Vogel et al., 2011). However, additional ubiquitin regulatory signals occur during oxidative stress that are independent of the proteasome. As the majority of enzymes in the ubiquitination cascade contain cysteine residues in their catalytic sites, these enzymes can undergo redox modifications such as formation of disulfides as well as sulfenic, sulfinic, or sulfonic acid (Netto et al., 2007) and have their activity regulated by reactive oxygen species (ROS) (Chung et al., 2013). Still, only a fraction of ubiquitinating and deubiquitinating enzymes seems to be affected by ROS, and the structural and sequence features determining their regulation remain elusive (Lee et al., 2013). In the RTU, we determined that redox inhibition of the DUB Ubp2 is essential for the accumulation of K63-ubiquitinated conjugates under stress (Silva et al., 2015). However, it is still unclear how ubiquitin-conjugating enzymes contribute to K63 ubiquitination of ribosomes and how their activity is regulated in response to oxidative stress.

In the canonical ubiquitination pathway, the E2-E3 interaction determines substrate specificity (Buetow and Huang, 2016), while the E2 is largely responsible for the ubiquitin chain topology extended on these substrates (Stewart et al., 2016). Deletion of Ubc13, the main E2 known for promoting K63-linked ubiquitination in yeast (Hodge et al., 2016), did not prevent the accumulation of K63-ubiquitinated proteins under stress (Silva et al., 2015), which suggests that additional E2s would be able to conjugate K63 ubiquitin chains to ribosomes during stress. We have shown that deletion of the E2 Rad6 impacted the accumulation of K63 ubiquitin chains under stress (Silva et al., 2015); it remained unclear, however, whether Rad6 directly modifies ribosomes and whether its activity is regulated by ROS. Furthermore, we lacked understanding on how deletion of *RAD6* impacts translation and cellular resistance to stress.

In this study, we set out to investigate the key role of Rad6 in regulating cellular response to stress in budding yeast as part of the RTU. Rad6 is small (20 kDa), highly conserved, and a multifunctional E2 involved in DNA repair and in the ubiquitination of substrates for the N-end rule pathway (Dohmen et al., 1991; Hoege et al., 2002). First, we found that Rad6 promotes K63 ubiquitination of ribosomes *in vitro* and *in vivo*. Using cryo-EM and molecular modeling, we identified key protein features important for enzyme-substrate

association. We also elucidated a negative-feedback mechanism by which Rad6 is redox inhibited in a reversible fashion by forming a disulfide with the E1 ubiquitin-activating enzyme (Uba1), thus limiting the amount of K63-ubiquitin modification. We further showed that Rad6 function in the K63 ubiquitination of ribosomes can be complemented by its human orthologue UBE2A, which can also be redox regulated by disulfide formation in human cells. To cope with the harms of oxidative stress, cells must orchestrate a global inhibition of translation while increasing the synthesis of antioxidant, repair, and stress-related proteins. Here, we showed that Rad6 is necessary for reprogramming translation and for adequate synthesis of antioxidant proteins, suggesting a central role for this E2 enzyme in protein synthesis during the stress response.

RESULTS

Rad6 is the E2 responsible for ribosomal K63-linked polyubiquitination

To understand the role of Rad6 in the RTU, we started by testing whether Rad6 was able to ubiquitinate ribosomes. We first showed that the expression of *RAD6* in the *rad6* mutant strain is sufficient to recover both its growth defect (Figures 1A and S1A) and the levels of K63 ubiquitin chains in the cell lysate and ribosome pellet (Figures 1B and 1C). Ribosome pellets were isolated by ultracentrifugation, here and henceforth, through a sucrose cushion. We also observed that neither the expression of Rad6^{C88S} nor Rad6^{C88A} mutants were able to rescue the K63-ubiquitination profile in the *rad6* mutant strain (Figure 1B). Noteworthy, Rad6^{C88S}, but not Rad6^{C88A}, likely forms an oxyester bond with ubiquitin instead of a dithiothreitol (DTT)-reducible thioester (Figure S1B). Next, we reconstituted an *in vitro* ubiquitination system, which showed that affinity-purified Rad6 is able to polyubiquitinate ribosomes (Figures 1D and S1C). Ubiquitination reactions were performed with ribosomes isolated from the *rad6 bre1* strain and were controlled for auto-ubiquitination of the system in the absence of ribosomes (Figures S1D and S1E). Rad6-mediated ubiquitination of ribosomes *in vitro* was observed in the absence of Bre1 (Figures 1D and S1D), the E3 ubiquitin ligase partner of Rad6 in the RTU (Silva et al., 2015). Rad6 has been shown to ubiquitinate substrates *in vitro* independent of E3 enzymes (Sung et al., 1988; Wu et al., 2011); however, deletion of Bre1 drastically reduces the levels of K63-ubiquitinated ribosomes in the cellular context (Figure 1E). These results indicate that Rad6 and Bre1 are necessary for K63 ubiquitination in the RTU pathway. Moreover, previous work has shown that Rad6 was able to transfer K63-linked ubiquitin chains directly to its substrate (Masuda et al., 2012). We confirmed that Rad6 can be charged by E1 and transfer K63-linked di-ubiquitin to ribosomes (Figures 1F and 1G) but fails to ubiquitinate ribosomes *in vivo* and *in vitro* in the presence of the K63R ubiquitin mutant that prevents the extension of K63-linked ubiquitin chains (Figures 1H and S1F). In addition, we also tested whether Ubc13 and Hel2 played a role in K63 ubiquitination in the RTU. Ubc13 and Hel2 are enzymes known to mediate in K63-specific ubiquitination (Hodge et al., 2016) and ubiquitination of ribosomes in quality-control pathways (Matsuo et al., 2017), respectively. We observed that ribosomes extracted from *ubc13D* and *hel2* were still modified by Rad6 *in vitro* (Figures S1G and S1H), and we found that deletion of *UBC13* and *HEL2* does not impair the levels of K63 ubiquitination in response to stress (Figures S1l and S1J). Thus, our results provide evidence

for a new role of Rad6 in ubiquitinating ribosomes and also reveal a new E2 enzyme able to participate in the conjugation of K63-linked polyubiquitin chains in yeast.

Acidic and hydrophobic regions of Rad6 regulate its co-sedimentation with ribosomes

We next sought to provide insights into the mechanisms by which Rad6 interacts with ribosomes to promote ubiquitination in the cellular context. Our previous structural data showed that fully assembled ribosomes are ubiquitinated in response to stress (Zhou et al., 2020a). We first confirmed that proteins from the 40S and 60S ribosome co-immunoprecipitate with FLAG-tagged Rad6 (Figure 2A). Rad6's presence in the ribosome pellet is not severely impacted by high salt concentration, thiol reducing agents, DNAse, or RNAse (Figure 2B), further indicating that Rad6 interacts with ribosomal proteins and not RNA or other associated proteins.

By performing polysome profiling analysis, we identified Rad6 present in the light (40S, 60S, 80S) and heavy (polysome) fractions of the sucrose gradient. First, we observed that Rad6's presence in the monosome and polysome fractions is not driven by H_2O_2 treatment (Figures S2A and S2B). This co-sedimentation pattern is also independent of the presence of the hemagglutinin (HA) tag (Figure S2B), of the N- or C-terminal location of the HA tag (Figure S2C), of Rad6 catalytic cysteine (Figure S2D), and of Rad6's known E3 ligases (Bre1, Ubr1, and Rad18) (Figure S2E). To confirm that Rad6's presence in the polysomal fraction is specific, we tested whether Rad6 has the capacity to carry other proteins to the heavy sucrose fractions. Although Rad6 and GFP are small proteins, we showed that GFP fused to Rad6, but not GFP alone, relocates to the polysome fraction *in vivo* (Figure 2C). Moreover, we found that purified Rad6 (but not purified GFP) relocates to the polysome fraction after incubation with isolated ribosomes *in vitro* (Figure 2D), suggesting that Rad6 is intrinsically able to interact with ribosomes. Finally, we observed that the RTU E3 Bre1 (Silva et al., 2015) is also present in the polysome fraction (Figure S2F), supporting a model that the RTU ubiquitin conjugase and ligase are associated with ribosomes to promote K63 ubiquitination.

The presence of Rad6 in the heavier fractions of the profile of unstressed cells (Figures 2C and S2A–S2E) suggests that Rad6 interacts constitutively with ribosomes instead of being actively recruited during oxidative stress. To gain insights on the molecular nature of Rad6's interaction with ribosomes, we applied cryo-EM analyses and characterized structural features related to ribosome ubiquitination in the RTU. Single-particle cryo-EM analysis of isolated ribosomes incubated *in vitro* with purified Rad6 (Ribo[Rad6mix]) showed five distinct classes distributed along different stages of elongation (Figures 2E and S3A). We were not able to observe density for Rad6, likely because of its small size, intrinsic flexibility, and number of potential binding sites. Alternatively, to enrich for the ribosomal fraction associated with Rad6 intracellularly, we co-immunoprecipitated ribosomes associated to FLAG-tagged Rad6 (Ribo[Rad6IP]) and subjected this sample to cryo-EM imaging (Figures S3B and S3C). Our analysis revealed that these ribosomes were present at the classic and the rotated pre-translocation stages of translation, containing densities for two tRNAs in the hybrid A/P (aminoacyl/peptidyl) and P/E (peptidyl/exit) positions (Figures 2E and 2F). Using focused classification, we identified two sub-classes for the 40S beak with

a conventional and extended version of the 18S rRNA, displaying a reorganization of the proteins eS31 and eS12 (Figures 2G and S3B). Focused classification of Ribo^{Rad6mix} showed a dynamic motion of the 40S beak including the K6 class with the extended beak (Figures S4A and S4B). To increase the stability of the complex, we cross-linked the Rad6-immunoprecipitated ribosomes (Ribo$^{Rad6IP-XL}$), which also revealed the extended form of the 40S beak (Figure S4C). To further understand whether these structural features were dependent on ubiquitination, we compared Ribo^{Rad6IP} with the structure of K63-ubiquitinated ribosomes and ribosomes extracted from the K63R ubiquitin mutant strain (Zhou et al., 2020a). Although we saw the same extended 18S rRNA conformation in all 3 datasets (Figures S4D and S4E), we observed a more dynamic behavior of the 40S beak (elongated density and multiple conformations) on K63 ubiquitinated ribosomes, while the K63R mutant dataset showed a combination of conventional and extended 40S beak conformations (Figures S4D and S4E). Our data suggest a model in which Rad6 would foster reorganization of the 40S beak with extension of the 18S rRNA by either binding or ubiquitinating lysine residues on localized ribosomal proteins such as eS12.

To gain further insights on Rad6 interaction with ribosomes, we carried out molecular-docking calculations and inspected the resulting models on the K63-ubiquitination sites of the 40S beak protein eS12, which showed distinctive conformational changes by cryo-EM (Figure 2G) and is known to be highly ubiquitinated under stress (Back et al., 2018). By considering constraints, such as the requirement for the Rad6 catalytic cysteine to be proximal to ubiquitinated lysine residues, we narrowed down the top-scoring models to a single, viable docking pose for the ubiquitination sites on eS12. These candidate poses placed the catalytic cysteine of Rad6 (C88) near the ubiquitinated lysine residues of eS12 (K85 and K90) and an acidic region of Rad6 (60-DEE-62) close to hydrophobic patches on the ribosome surface (Figures 3A and S4F). Additional Rad6 residues close to the catalytic cysteine (N84, N94, Y82) were also predicted to contribute to Rad6 binding to the ribosomal surface (Figure 3A). Finally, our model also predicted interactions between the C-terminal residues of Rad6 and the ribosome. To validate our molecular-docking predictions, we mutated Rad6's residues and domains that would support its interaction with the ribosomal protein surface (Figure 3B). In agreement with the docking analysis, mutation to Rad6's acidic region to a hydro-phobic stretch (DEE60-62LLL, hereafter named Rad6^{LLL}) fostered Rad6's association with ribosomes fractions, with higher localization to the 80S fraction (Figure 3C). Moreover, mutation to Rad6 N84 and N94 to hydrophobic residues Rad6^{N84L}, Rad6^{N84A}, and Rad6^{N94L} also increased co-sedimentation of Rad6 with ribosomes (Figures 3D and 3E). We also identified domains that reduce Rad6's presence in the ribosome pellet. Removal of Rad6's acidic tail (denoted Rad6$^{1-149}$), which is known to stabilize Rad6's interaction with substrates (Raboy and Kulka, 1994; Sung et al., 1988), decreased Rad6's presence in the polysomes (Figures 3F and S5A) and ribosome pellet (Figure 3G). Subsequent removal of Rad6's last alpha helix (denoted Rad6$^{1-122}$) drastically reduced its presence in the heavy polysome fraction (Figures 3FH and S5B). Both, Rad6$^{1-149}$ and Rad6^{LLL}, but not Rad6$^{1-122}$, were capable of ubiquitinating ribosomes and complement the growth defect of *rad6*Δ (Figures S5C–S5G). Although Rad6$^{1-122}$ has a reduced presence in the polysome fraction, this isoform still retains its capacity to be charged with ubiquitin (Figure S5H) and offers partial resistance to DNA replication stress

(Figure S5I). Using a combination of structural biology, molecular-docking analysis, and cellular assays, we identified a series of amino acids and domains involved in Rad6 function and association with ribosomes in the RTU, providing new understandings on the enzyme-substrate relationship for this multifunctional E2.

Rad6 is redox regulated by hetero-disulfide formation with Uba1

We have previously shown that K63 ubiquitin chains accumulate in ribosomes because of redox inhibition of the deubiquitinating enzyme Ubp2 (Silva et al., 2015). Rad6 is a cysteine-based enzyme that can also be affected by ROS, but the regulation of Rad6 under oxidative stress remained unexplored. Following cellular treatment with H_2O_2, we observed the formation of a Rad6-containing high molecular weight complex on non-reducing blots of isolated ribosomes (Figure 4A). This complex is reducible by DTT and depends on Rad6's catalytic cysteine. Its formation is impaired by high salt concentration and by the cysteine-alkylating agent iodoacetamide (IAM) (Figures 4B, 4C, and S6A), which suggests the formation of a hetero-disulfide. We reasoned that in response to stress, Rad6 forms a disulfide complex with proteins with which it closely interacts, such as ribosomal proteins or enzymes from the ubiquitination cascade. First, we showed that this disulfide is not formed with a single Rad6-interacting E3 (Figure S6B). Therefore, we performed denaturing co-immunoprecipitation of Rad6 under stress conditions to identify Rad6's redox partner (Figure 4D). Using stable-isotope labelling by amino acids in cell culture (SILAC)-based quantitative mass spectrometry (Ong et al., 2002) on the DTT-eluted fraction, we unambiguously determined that Uba1, the yeast E1 activating enzyme, was the major binding partner of Rad6 during H_2O_2 stress (Figure 4E). We validated that Uba1 was *a bona fide* Rad6 redox partner by showing that Rad6, but not Rad6[C88S], co-immunoprecipitates with Uba1 and is released upon DTT reduction (Figure 4F). Although other ubiquitin-conjugating enzymes could interact with Uba1 and form Cys-based complexes during oxidative stress, first we showed that the K63-linked specific E2 Ubc13 is unable to form disulfides with UBA1 even under *in vitro* conditions (Figure S6C). Moreover, we showed that Rad6 is the most abundant Uba1 partner in our *in vivo* system. Yeast cells expressing the mutant Rad6[C88S] do not show detectable levels of other Uba1 hetero-disulfides following H_2O_2 treatment (Figure 4G). Supporting our findings, Rad6 mutants with reduced Uba1 interactions (such as Rad6[R7A] and Rad6[R7A/R11A]) (Tokgoz et al., 2012; Williams et al., 2019) are less able to form disulfides in response to stress (Figures 4H and S6D).

We also found that the Rad6-Uba1 complex rapidly disappears during cellular recovery from stress (Figure S6E). Inhibition of the proteasome or autophagy did not increase the stability of the Rad6-Uba1 complex (Figures S6E and S6F), and a pulse-chase experiment showed that Rad6 is not degraded after stress induction (Figures S6G and S6H). Thus, these results suggest that thiol reductases are involved in the reduction and recycling of these enzymes. By screening an array of mutants, we showed that deletion of glutathione reductase (*GLR1*) impaired the reduction of Rad6-Uba1 disulfide during stress recovery (Figures 4I and S6I), while genes from the thioredoxin family had no detectable effect on disulfide reversal (Figures S6J and S6K). A concomitant treatment with the inhibitor of glutathione synthesis, buthionine sulphoximine (BSO), in the *glr1* background strongly prevented the reduction

of the disulfide (Figure 4J). Collectively, our data support a mechanism by which Rad6-Uba1 is formed following stress induction and is rapidly reversed by glutathione-dependent enzymes once cellular reductive capacity is restored.

To further investigate the mechanism of Rad6 disulfide formation, we used an *in vitro* assay that indicated that Rad6 acts as the redox sensor of the pair. Prior oxidation of Rad6 leads to significantly increased formation of the Rad6-UBA1 complex when compared with prior oxidation of UBA1 alone or of both enzymes (Figure 5A). Supporting this chemical regulatory mechanism, formation of Rad6-containing disulfides would depend on the stabilization of a reactive thiolate group in its Cys88. Rad6 oxidation by H_2O_2 is able to produce a stable sulfenic acid (Figure 5B), which would serve as intermediate for the Rad6-Uba1 disulfide formation. By inspecting the Rad6 catalytic site (Kumar et al., 2015), we observed three conserved residues able to affect the C88 thiolate stability: N80, Y82, and Q93 (Figures 5C and S6L) (de Oliveira et al., 2019). Mutations to these residues still allowed these Rad6 variants to be charged by Uba1 with ubiquitin at different extents (Figure 5D). However, while a Q93E mutant partially reduced the accumulation of K63-ubiquitinated targets, the Q93R and N80A mutants severely impaired the accumulation of K63 ubiquitin chains and their capacity to form disulfides under stress (Figure 5D). These findings suggest a key role for Rad6 thiolate in the formation of Rad6-Uba1 disulfide and in the regulation of cellular response to oxidative stress. Supporting the notion that formation of the Rad6-Uba1 complex is an endogenous process, we detected its presence at low abundance even in the absence of stress (Figure S6M). Although we showed that exogenous H_2O_2 treatment heightens the formation of this complex, generation of intracellular ROS by methyl methanesulfonate (MMS) (Kitanovic et al., 2009) also increases the levels of the Rad6-Uba1 complex and leads to an accumulation of K63 ubiquitin conjugates (Figure S6N).

Although we have characterized the mechanism by which Rad6 activity is regulated by oxidative stress induced by H_2O_2, it poses a paradox since oxidative stress leads to the accumulation of K63 ubiquitin while inhibiting Rad6 activity by using its single cysteine residue to form a disulfide complex with Uba1. In this context, we postulated that Rad6 would first ubiquitinate ribosomal proteins and subsequently be oxidized and inhibited by disulfide formation. In agreement with this hypothesis, a time course experiment showed that K63 ubiquitin chains accumulated as early as within 2 min of stress induction followed by a subsequent accumulation of the Rad6-Uba1 complex(Figure 5E). In addition, we observed that increased formation of the Rad6-Uba1 complex correlates with the depletion of the pool of free ubiquitin (Figures 5E and 5F). We proposed that depletion of the ubiquitin pool would allow a prolonged interaction of Rad6 and Uba1, which would in turn support the formation of the redox disulfide. To validate this hypothesis, we conducted *in vitro* oxidation assays and confirmed that the presence of increased amounts of ubiquitin largely reduced the formation of the Rad6-Uba1 complex. The use of PYR-41, a selective and irreversible inhibitor of the E1 active site (Yang et al., 2007), completely blocked the formation of the Rad6-Uba1 complex *in vitro* (Figure 5G). The proposed role of free ubiquitin in affecting the levels of the Rad6-Uba1 complex *in vivo* was further strengthened by the use of mutant strains deleted for DUBs known to decrease the levels of free ubiquitin (Hanna et al., 2003) (Figure S6O). Conversely, cells grown to stationary phase,

which physiologically contain high amounts of ubiquitin, showed increased levels of K63 ubiquitination, no depletion of the pool of free ubiquitin, and no accumulation of Rad6-Uba1 disulfides *in vitro* or *in vivo*, even at acute 2.5 mM H_2O_2 treatment (Figure 5H). The Rad6-Uba1 complex supports a negative feedback loop in which early formation of disulfides upon reduced ubiquitin levels limits the amount of K63 ubiquitin conjugated to ribosomes due to Rad6 inhibition (Figure 5I). We tested this model by using the yeast strain carrying Rad6$^{R7A/R11A}$, the mutant that has reduced interaction with Uba1 (Tokgoz et al., 2012) and forms low amounts of redox disulfide with Uba1 under stress (Figure 4H). The Rad6$^{R7A/R11A}$ strain displayed higher levels of K63 ubiquitination during the progression of stress (Figure 5J) and was able to accumulate more K63 ubiquitin conjugates when subjected to increased H_2O_2 concentrations (Figure 5K). These findings suggest that the formation of Rad6-Uba1 disulfides is a critical piece of a negative feedback loop needed to regulate the levels of K63 ubiquitination and cellular response to stress.

We next asked whether this redox regulation of Rad6 and its ability to build K63 ubiquitin chains is evolutionarily conserved in higher eukaryotes. Expression of Rad6 homologs in the *rad6* background has been shown to recover DNA repair functions but not all phenotypes (Koken et al., 1991a, 1991b). Episomal expression of the human homolog of Rad6 (UBE2A) in the *rad6* background recovers its defective growth phenotype. induces stress resistance, and promotes K63 ubiquitination of ribosomes (Figures 6A, 6B, S7A, and S7B). UBE2A also co-sediments with ribosomes (Figures 6C and 6D) and is able to form disulfides during stress when expressed in yeast and also natively in HeLa cells exposed to H_2O_2 (Figures 6E, 6F, and S7C). Thus, our results suggest that redox ubiquitination of ribosomes can be performed by Rad6 or-thologues and that the formation of Rad6-containing disulfides is evolutionarily conserved and regulates UBE2A function in human cells exposed to oxidative stress.

Rad6 is required for translation reprogramming under stress

In the RTU, we showed that K63 ubiquitin chains participate in the regulation of translation elongation in response to oxidative stress (Zhou et al., 2020a). However, the impact of Rad6 in translation and cellular resistance to stress remained underexplored. Similar to K63 ubiquitin chains (Back et al., 2018), *RAD6* is necessary for global inhibition of translation that occurs under cellular exposure to H_2O_2 (Figures 7A and S7D). Furthermore, wild-type cells exposed to H_2O_2 showed significant inhibition of translation measured by a GFP reporter system, while the rate of GFP production remained mostly unchanged in *rad6* cells (Figure 7B). As expected, wild-type cells reduce their growth rate upon stress induction, and following adaptation to this new environment, they resume exponential growth and achieve stationary phase. However, *rad6* cells showed a distinct growth pattern, with a faster increase in optical density than the wild type during early exposure (<10 h) to H_2O_2 treatment (Figures 7C and S7E). These results suggest that *rad6* cells are either more resistant to H_2O_2, do not sense H_2O_2, or do not respond properly to the insult. To test these hypotheses, we first determined that *rad6* cells have higher levels of ROS than wild type at steady state, which increases significantly after 30 min of stress induction (Figure 7D). This result indicates that *rad6* cells are sensitive to H_2O_2 treatment. Flow cytometry analysis showed that H_2O_2 treatment led to similar arrest in cell division in the wild-type

and *rad6Δ* cells (Figure S7F); however, *rad6Δ* cells displayed a prevalence of relatively larger cells than wild type under stress (Figure S7G). These findings indicate that *rad6Δ* cells are able to sense H$_2$O$_2$ and that its increased relative size is likely associated with active (unrepressed) translation, thus suggesting that *rad6Δ* cells do not respond properly to oxidation insults. To understand Rad6's impact on protein production, we employed quantitative mass-spectrometry analysis and observed that after normalization by strain differences, only a few proteins were differentially expressed in *rad6Δ* compared with wild-type cells during stress (Figure 7E). We also observed that several stress-related proteins increase in abundance upon stress induction in both strains (Figure 7F). Our previous analysis (Figures 7A and 7B) showed increased protein production in *rad6Δ* cells under stress, suggesting that this strain would accumulate high levels of stress-related proteins over time. As predicted, *rad6Δ* cells show higher levels of Tsa2, Gpx2, and Sod2, of which the high levels also lasted longer than in the wild type (Figure 7G). By qPCR analyses, we showed that both strains present similar transcriptional induction for these genes, reinforcing the role of Rad6 in translational control (Figure 7H). Collectively, these findings suggest that both stains, wild type and *rad6Δ*, induces the expression of similar antioxidant programs at the transcriptional level but that the differences are rather quantitative and time dependent at the translational level (Figure 7G). Therefore, our results support the model that the lack of K63 ubiquitination mediated by Rad6 during stress prevents proper regulation of translation, leading to increased cell size, stress sensitivity, and dysregulated expression of antioxidant proteins.

DISCUSSION

Our work characterized a redox function for the ubiquitin-conjugating enzyme Rad6 in the pathway of RTU. In the RTU, we showed that Rad6 co-sediments (Figures 2A–2C) and modifies ribosomes with K63 polyubiquitin chains (Figures 1B–1D, 1G, and 1H). Even though structural analysis of co-immunoprecipitation of ribosomes with associated factors generally retrieves a low percentage of particles bound to the interactors (Gamerdinger et al., 2019; Pochopien et al., 2021), our cryo-EM data indicate that Rad6 associates with ribosomes at the pre-translocation stage of elongation. This association can then lead to alterations in the 40S beak structure (Figures 2E–2G), promoted by either binding or activity of Rad6. As predicted by our docking calculations (Figure 3A), we identified Rad6 residues and domains that affect its activity and interaction with ribosomes (Figures 3C–3G and 5D). Interestingly, the Rad6 C-terminal acidic tail has been shown to be required for polyubiquitination of histones and to offer a mechanism for the attachment of multiple Rad6 molecules to the substrate (Sung et al., 1988). In agreement, our data suggest that this acidic tail could provide a conserved mechanism by which multiple Rad6 molecules interact with other large basic complexes, such as the ribosome. This model, based on electrostatic interactions, could also explain how Rad6 can ubiquitinate fairly distant ribosomal proteins.

We also showed that this K63 ubiquitination is independent of Ubc13, the main E2 involved in selective formation of K63 ubiquitin linkages (Hodge et al., 2016) Figure S11). Interestingly, it has been suggested that Rad6 could transfer K63 ubiquitin chains *en bloc* to its substrate proliferating cell nuclear antigen (PCNA); however, these K63 ubiquitin chains were still built by Ubc13 (Masuda et al., 2012). Here, we showed that Rad6 can be charged

and transfer K63-linked chains directly to substrates (Figures 1F and 1G). Moreover, this burst of K63 ubiquitination under stress is independent of the E2 Ubc4 (and its paralog Ubc5) (Silva et al., 2015) and of the E3 Hel2 (Figure S1J), which has been suggested as the E2 and E3 involved in ribosome ubiquitination in quality-control pathways (Inada, 2013; Joazeiro, 2019; Matsuo et al., 2017; Sugiyama et al., 2019). Thus, our results suggest that Rad6 modifies ribosomes in the RTU, independent of other pathways of translation control, illustrating a potential functional code for ribosome ubiquitination. It is likely that these pathways occur concomitantly in a complex and dynamic environment, targeting different subpopulation of ribosomes with distinct ubiquitin linkages, with Rad6 carrying out most of the K63 ubiquitination load during oxidative stress.

Our model proposes that the DUB Ubp2 acts as a stress sensor in the RTU, whose inhibition by H_2O_2 leads to the accumulation of K63-ubiquitinated ribosomes. This model assumes that ubiquitination and deubiquitination of ribosomes are integral components of the translation cycle and that K63 ubiquitin chains accumulate when deubiquitination is impaired or overwhelmed. This model is supported by the constitutive presence of Rad6 on ribosomes (Figure 2C) and by the fact that increased translation initiation leads to higher levels of K63 ubiquitination even in the absence of stress (Silva et al., 2015). Moreover, the lack of K63 ubiquitination impacts polysome stability and renders cells more susceptible to translation inhibitors in the absence of stress (Silva et al., 2015; Spence et al., 2000); however, the mechanisms underlying these processes remain elusive.

Several enzymes can be modified by ROS in a redox-switch manner to rapidly regulate their function (Brandes et al., 2009; Topf et al., 2018). Although many of these enzymes contain catalytic cysteine residues, their susceptibility to oxidation requires a structural organization that renders a reactive thiolate group (Netto et al., 2007) and a conducive cellular environment that fosters the formation of oxidized species. For example, it has been shown that only a fraction of DUBs from the cysteine-containing USP family can be redox regulated and re-activated by DTT (Lee et al., 2013; Snyder and Silva, 2021). Cysteine-oxidation events can be observed in the yeast proteome (~4,300 Cys, ~7.5% of all yeast cysteines); however, only 0.3% of these residues were identified as disulfides (Topf et al., 2018). These authors identified many E2s that could be oxidized under stress; however, their potential to form disulfides with Uba1 is still unclear. Previous work had proposed that the yeast Cdc34 would be the only E2 oxidized after diamide or high H_2O_2 concentration (2 mM) in rich medium (Doris et al., 2012). Here, we showed that Rad6 is redox regulated (Figure 4B) and is the main protein forming disulfides with Uba1 during peroxide stress in our system (Figures 4E–4G). We also showed that the human homolog of Rad6 (UBE2A) complements Rad6 function and is redox regulated in yeast and in HeLa cells (Figure 6). Considering Rad6's structural features, we demonstrated that residues that foster Rad6's interaction with the Uba1 (R7 and R11) and conserved residues such as N80 and Q93 are important for Rad6 activity and its capacity to form disulfides (Figures 4H and 5D). We further showed that Rad6-Uba1 disulfide formation depends on the pool of free ubiquitin, which acts in a negative feedback loop to regulate the levels of K63 ubiquitination (Figures 5E–5K). This mechanism would also prevent a complete depletion of the pool of free ubiquitin, given the abundance of ribosomes. Our data suggest that Rad6 interaction with uncharged Uba1 would favor a conformation that exposes their cysteine residues and

fosters the formation of a disulfide bond in the presence of H_2O_2. Furthermore, we showed that the Rad6-Uba1 complex is not degraded during recovery from stress and that it requires the glutathione system to be reversed in the cellular context (Figures 4I and S6E–S6I). We speculate that formation of this Rad6-Uba1 disulfide protects these enzymes from hyperoxidation, and the reversibility of this process would allow cells to quickly recycle and utilize these enzymes.

In the RTU, K63 ubiquitination is required to inhibit translation during stress (Back et al., 2018; Silva et al., 2015). K63 ubiquitin chains modify fully assembled ribosomes, and these complexes were mostly present in the pre-translocation stage of elongation, with a marked destabilization of the 60S P-stalk (Zhou et al., 2020a). Here, we showed that *RAD6* is required for global inhibition of translation during cellular exposure to H_2O_2 (Figures 7A and 7B) and could also induce structural changes in the highly ubiquitinated 40S beak (Figure 2G). We reasoned that dysregulation of translation by the absence of K63-ubiquitinated ribosomes renders cells more sensitive to stress (Figures 7C and 7D). To survive the harms of oxidative stress, wild-type cells reprogram translation by downregulating protein synthesis globally while producing in a timely manner proteins that are critical for stress resistance (Grant, 2011). However, *rad6* showed continuous protein production under H_2O_2, including dysregulated levels of antioxidant enzymes (Figures 7A, 7B, and 7G), which suggests a critical role for Rad6 in the regulation of translation under stress.

Finally, Rad6 is a highly conserved protein whose mutations in higher eukaryotes have been associated with cognitive and learning deficits (Bruinsma et al., 2016) and in humans have led to the intellectual disability type Nascimento (Nascimento et al., 2006) and the progression of chronic myeloid leukemia (Magistroni et al., 2019). UBE2A also binds the E3 ligase Parkin, which ubiquitinates proteins involved in the clearance of defective mitochondria (Haddad et al., 2013). Mutations to UBE2A Arg7 have been identified in individuals with Nascimento syndrome (Czeschik et al., 2013). We have shown that the mutant Rad6$^{R7A/R11A}$ has impaired capacity to form disulfides and dysregulated K63 ubiquitin responses (Figures 4H, 5J, and 5K). Previous studies have shown a spectrum of clinical phenotypes for Nascimento syndrome depending on the UBE2A mutation carried by these individuals (Czeschik et al., 2013). The different domains that control UBE2A activity, protein interaction, and translation control could provide important ways to explain this range of phenotypes. Defining the role of UBE2A domains, their function in translation reprogramming, and their effect in stress response will be key to understanding the progression of, as well as cellular resistance against, many stress-related diseases.

Limitations of the study

A limitation of the study is that we lack a refined model of Rad6 interaction with ribosome to modify its proteins under stress. Our data provide molecular, cellular, and structural evidence that will continue to inform the elucidation of the model. It also remains to be determined how applicable some of the mechanisms proposed here will be to other E2s, cellular pathways, and organisms. Finally, another limitation is that the mechanism by which ubiquitin, conjugated by Rad6, induces translation arrest and impacts the reprograming

of gene expression remains elusive. Additional work must be performed to elucidate the functional sites of ubiquitination affecting translation under stress.

STAR★METHODS

RESOURCE AVAILABILITY

Lead contact—Further information and requests for resources and reagents should be directed to and will be fulfilled by the lead contact, Gustavo Silva (gustavo.silva@duke.edu).

Materials availability—All unique/stable reagents generated in this study are available from the lead contact with a completed Materials Transfer Agreement.

Data and code availability—Two Ribo^{Rad6IP} EM maps were deposited in the Electron Microscopy DataBank (EMDB), https://www.ebi.ac.uk/pdbe/emdb displaying the conventional (Accession no. EMDB: EMD-26440) and the extended conformation of the 40S beak (Accession no. EMDB: EMD-26441). Maps are publicly available as of the date of publication. Accession numbers are listed in the Key resources table.

The mass spectrometry proteomics data have been deposited to the ProteomeXchange Consortium via the PRIDE partner repository and are publicly available as of the date of publication. Accession numbers are listed in the Key resources table.

This paper analyzes existing, publicly available data. These accession numbers for the datasets are listed in the Key resources table.

This paper does not report original code.

Any additional information required to reanalyze the data reported in this work paper is available from the lead contact upon request.

EXPERIMENTAL MODEL AND SUBJECT DETAILS

Microbe strains—All yeast *Saccharomyces cerevisiae* strains used in this study are described in Table S3. Unless specified, yeast cells were cultivated into synthetic dextrose minimal medium (SD: 0.67% yeast nitrogen base, 2% dextrose and required amino acids) at 30°C at 200 rpm agitation.

E. coli strains used in this study were NEB10-beta and BL21-CodonPlus (DE3)-RIL grown into LB-medium.

Cell lines—HeLa cell line was obtained from the ATCC (ATCC CCL2). HeLa cells (ATCC CCL2) were cultured in EMEM (ATCC 30-2003) containing 10% fetal bovine serum (Invitrogen 16,140,071) and 1% Penicillin/Streptomycin (Invitrogen 15,140,122) and incubated at 37°C and 5% CO_2.

METHOD DETAILS

Strain generation and protein extraction—Standard recombination methods were used to delete and tag genes; deletions were confirmed by PCR and tagged genes were

confirmed by PCR and immunoblotting. Cas9-mediated gene editing was used to create a Rad6[R7A/R11A] strain as described elsewhere (Ryan et al., 2016). gRNA sequence used to target Rad6 and the donor sequence for the point mutations are described in the Key resources table. All plasmids and selected oligonucleotides used in this study are listed in Table S4. Cells were disrupted by glass-bead agitation at 4°C in standard buffer: 50 mM Tris-HCl pH 7.5, 150 mM NaCl, 20 mM iodoacetamide (IAM), 1X protease inhibitor cocktail set I (Millipore-Sigma). Mammalian cells were treated with 500 μM H_2O_2 at 70% confluence one day after being seeded. Protein extraction was performed by cell sonication in standard buffer containing 0.5% NP40. Extracts were cleared by centrifugation, and protein concentration was determined by Bradford assay (Bio-Rad) prior to western blotting.

Growth assays

Growth curve determination: Yeast cultures were grown into SD medium to mid-log phase and back-diluted to OD_{600} 0.1. Equal volumes of cell suspension and fresh SD medium (75 μL) were added to a 96-well plate in triplicate. Plates were incubated at 30°C with shaking, and absorbance was measured at 595 nm every 15 min in a Tecan Sunrise microplate reader.

Sensitivity assays: Indicated strains were grown into SD medium to mid-log phase and back-diluted to OD_{600} of 0.1. Serial five-fold dilutions were spotted onto YPD plates and incubated for 2 days at 30°C.

Protein purification—Rad6, Bre1, and Ubc13: Proteins were expressed in pGEX vector containing GST-tag and TEV protease sequences. Expression of recombinant proteins was induced in *E. coli* BL21-CodonPlus (DE3)-RIL with 0.6 mM isopropyl thio-β-galactopyranoside (IPTG) for 4 h at 37°C (Rad6 and Ubc13) or overnight at 16°C (Bre1). Cells were lysed by sonication in NETN buffer (50 mM Tris-HCl pH 7.5, 150 mM NaCl, 0.5% IGEPAL) with 0.15 mM DTT, 1 mM PMSF, and lysozyme (10mg/mL). Lysate was cleared by centrifugation at 12,000 x g for 20 min at 4°C. Glutathione agarose resin (Goldbio G-250-5) was pre-washed with NETN buffer (3x) and incubated for 2 h at 4°C under rotation with the cleared lysate. Beads were washed twice with NETN buffer followed by two washes with 1X PBS buffer. Proteins were eluted by cleavage of the GST tag by 15 units/mL TEV protease (Sigma T4455-1KU) in PBS buffer overnight at 4°C. The eluted proteins were desalted using a PD-10 desalting column (Cytiva) in 50 mM Tris-HCl pH 7.5, 100 mM NaCl buffer.

Ubiquitination assays

Rad6 charging assay: Rad6 activity was assessed through an *in vitro* ubiquitin thioester assay in the presence of E1 UBA1 (20 nM), Rad6 (500 nM), ubiquitin (6 μM), and reaction buffer (20 mM HEPES pH 7.2, 10 mM $MgCl_2$, 1 mM DTT, and 10 mM ATP). The reaction was incubated at 37°C for 30 min and stopped with the addition of 4X Laemmli buffer.

Ubiquitination reactions: Assays were performed in the presence of 100 nM E1 UBA1 (Enzo Life Sciences BML-PW8395-0025), 250 nM Rad6, 150 nM of Bre1, 2-10 μM of ubiquitin (LifeSensors si201), 10 μg of isolated ribosomes, and energy regenerating system

(ERS – 1 mM ATP, 10 mM creatine phosphate, 20 μg/mL creatine kinase). All components were pre-incubated in reaction buffer (50 mM Tris-HCl pH 7.5, 150 mM NaCl, 2 mM MgCl$_2$, and 1 mM DTT) for 10 min at room temperature, before the addition of Bre1 and ribosomes. The reaction was incubated for up to 3 h at 30°C at 300 x rpm agitation and stopped by the addition of Laemmli buffer. When indicated, samples were incubated with 20 mM DTT for 10 min prior to western blotting.

Western blotting—Proteins were separated by standard 10 - 15% SDS-PAGE loaded in Laemmli buffer. Samples were transferred to PVDF membrane (ThermoFisher), and immunoblotting was performed using the following antibodies: anti-K63 ubiquitin (1:4,000; EMD Millipore, cat. no. 05-1308, clone apu3), anti-actin (1:6,000; Cell Signaling, cat. no. 4967), anti-GAPDH (1:4,000; Abcam, cat. no. ab9485), anti-Myc (1:5,000; ThermoFisher, cat. no. R950-25 and PA1-981), anti-Rad6 (1:8,000; Abcam, cat. no. ab31917), anti-Rps3/uS3 (1:6,000; Cell Signaling, cat. no. 9538S), anti-Rpl11/uL5 (1:6,000; Cell Signaling, cat. no. 18163S), anti-HA (1:10,000; ThermoFisher, cat. no. 71-5500), anti-Rps20/uS10 (1:9,000; ThermoFisher, cat. no. PA5-75383), anti-ubiquitin (1:10,000; Cell Signaling Technology cat. No. 3936S), anti-FLAG (1:3,000; MilliporeSigma, cat. no. F3165), anti-puromycin (1:4,000; MilliporeSigma, cat. no. MABE343), anti-ubc13 (1:1,000; Novus Biologicals, cat. no. NBP1-76593). Anti-mouse IgG (1:8,000-12,000; Cytiva, ca. no. NA931), anti-rabbit IgG (1:6,000-12,000; Cytiva, cat. no. NA934), and anti-mouse IgG2a (1:10,000-1:12,000; Abcam, cat. no. ab97245) secondary antibodies conjugated with HRP and ECL Prime detection reagents were acquired from Cytiva. All antibodies have been validated by the manufacturer or are expected to react with the species used in this study based on sequence similarity.

Sucrose density sedimentation analysis—Yeast cells were incubated in the presence of 150 μg/mL cycloheximide for 5 min at 30°C and lysed immediately in extraction buffer (20 mM Tris-acetate, pH 7.0, 50 mM NaCl, 15 mM MgCl$_2$, 20 mM IAM, 200 μg/mL heparin, 150 μg/mL CHX, 1x complete mini EDTA-free protease inhibitor cocktail (Roche). A total of 400 μg of RNA was sedimented by ultracentrifugation for 150 min at 36,000 rpm (Beckman SW40 rotor) at 4°C in a 7–47% sucrose gradient (buffered in 50 mM Tris-acetate, pH 7.0, 15 mM MgCl$_2$, 150 μg/mL CHX). During sucrose gradient analysis, sample absorbance was monitored at 254 nm while fractions were collected using a Brandel density gradient fractionation system equipped with the PeakChart software. Proteins from fractions were precipitated with TCA-acetone prior to immunoblotting.

Ribosome sedimentation—Yeast cells were lysed as for the sedimentation profile. A total of 400 μg of RNA (determined by A$_{260}$) was sedimented by ultracentrifugation for 120 min at 70,000 rpm (Beckman Optima Max-TL, TLA-110 rotor) at 4°C in a 50% sucrose cushion buffered in 50 mM Tris-acetate, pH 7.0, 150 mM NaCl, and 15 mM MgCl$_2$. Ribosome pellet was resuspended in 50 mM Tris-acetate, pH 7.0, 150 mM NaCl and ribosome-free supernatant was precipitated with TCA-acetone, followed by resuspension to the same final volume prior to immunoblotting.

Cryo-electron microscopy analysis

Sample preparation: 1) *Ribosome isolation for in vitro incubation with Rad6 (Ribo^{Rad6mix})*: Yeast cell lysate from *rad6* strain was prepared as above and ribosome pellets were resuspended in buffer containing 50 mM Tris-Acetate pH 7.0, 150 mM NaCl, 30 mM MgCl$_2$. 20 µg of ribosomes were incubated with 1.2 µM of purified Rad6. *2) Ribosome co-immunoprecipitation with Rad6-FLAG (Ribo^{Rad6IP})*: Yeast cell lysate from Rad6-FLAG strain (GMS488) was cleared by centrifugation and loaded into a column containing M2 anti-FLAG resin (Sigma-Aldrich). The sample was eluted with 100 µg/mL of 3X FLAG peptide (Sigma-Aldrich) in buffer containing 50 mM Tris-HCl pH 7.5, 100 mM NaCl, 5 mM MgCl$_2$, and 10% glycerol. Enrichment for large complexes and sample concentration was performed using Amicon centrifugal filter units with 100 kDa cutoff. Rad6-FLAG bound ribosomes were confirmed by immunoblot prior to cryo-EM analysis. *3) Cross-linking of ribosomes co-immunoprecipitated with Rad6-FLAG (Ribo$^{Rad6IP-XL}$)*: Ribo^{Rad6IP} prepared as above were incubated with 500 µM BS^3 (ThermoFisher) for 2h at 4°C.

Grid preparation: For Ribo^{Rad6IP} and Ribo$^{Rad6IP–XL}$, 3 µL of the samples at 1 µg/µL was applied to UltrAUfoil R1.2/1.3 grids (Quantifoil Micro Tools GmbH). Grids were glow-discharged for 30 s at 15 mA prior to sample application (PELCO easiGlow, Ted Pella, Inc.). Grids were blotted between 2.5 and 3 s and plunged frozen in liquid ethane using a Leica vitrification plunger (EM GP2, Leica Microsystems). For Ribo^{Rad6mix}, cryo-grids were prepared by rapid immersion into liquid ethane with a Vitrobot Mark IV (Thermo Fisher Scientific) set to 22°C and 95% humidity. Quantifoil 300 mesh R1.2/1.3 grids were used and glow-discharged as above.

Data collection: Ribo^{Rad6mix} and Ribo^{Rad6IP} micrographs were recorded under low-dose conditions on a FEI Titan Krios electron microscope (ThermoFisher Scientific) equipped with a K3 direct electron detector using the Latitude software (Gatan, Pleasanton, CA). A single hole was targeted per stage movement, and one shot was used per hole. Sixty frames at a nominal pixel size of 1.08 Å were collected per movie. The cumulative electron dose was 60 e$^−$/Å^2, and 3,062 movies and 7,872 movies were collected for Ribo^{Rad6IP} and Ribo^{Rad6mix}, respectively. Ribo$^{Rad6IP–XL}$ data were collected using SerialEM (Mastronarde, 2005) on a Talos Arctica microscope (ThermoFisher Scientific) equipped with a K2 detector. Data was collected at a magnification of 450,00x(0.932 Å/pixel). Movies were collected using a dose rate of ~0.8 e$^−$/Å^2/frame and a total of 60 frames were acquired over an 8.4 s exposure. A total of 3,372 movies were collected using 9 beam-image shift exposures per stage movement (3 x 3 hole pattern).

Single-particle data processing: For Ribo^{Rad6mix}, movie alignment was performed on-the-fly (Zhou et al., 2020b), and the contrast transfer function was determined on the motion-corrected sum of frames using CTFFIND4.1 (Rohou and Grigorieff, 2015). Micrographs were imported into cryoSPARC (Punjani et al., 2017) for particle picking and 2D classification. Around 1 M particles were selected and re-extracted with a binning factor of 4 (pixel size 4.32 Å) in RELION (Zivanov et al., 2018) for further processing. Another round of 2D classification was done in RELION resulting in 651,713 particles which

were subjected to 3D classification without masking. After removing the noise classes, the remaining 458,977 particles were re-extracted using a binning factor of 2 (pixel size 2.16 Å) and subjected to 3D refinement resulting in a map of 4.4 Å resolution. Polishing was performed to correct for the local motion of all refined particles. At this point, two different strategies were employed. First, we carried out focused classification to analyze the conformational changes of the 40S beak. All polished particles were refined with a shape mask only including the 40S domain. An elliptical shape mask located at the 40S beak region was then used for focused classification into six classes (Figure S4A). All classes were selected and used for 3D reconstruction without alignment to visualize the overall ribosome structure. For global classification, all polished particles were imported into cisTEM (Grant et al., 2018) and local 3D classification was performed using the refinement parameters obtained from RELION. Four classes (out of a total of six) showed well-defined tRNA features.

For the Ribo^{Rad6IP} dataset, all the data processing was done in RELION. A total of 245,077 particles were picked and extracted with a pixel size of 1.8 Å. Next, 224,217 particles were selected after 2D classification and subjected to 3D classification without masking. Three good classes consisting of 68,538 particles were selected and refined to 4.5 Å. Further 3D classification without alignment resulted in two different conformations of ribosomes (rotated PRE translocation state and classical PRE translocation state) and one noise class. For the 40S focused classification, all good 3D classes were pooled and re-extracted using a pixel size of 1.08 Å. Then, 3D refinement with a 40S shape mask was performed to align exclusively the 40S domain. Another round of 3D classification was conducted with an elliptical shape mask focusing on the 40S beak yielding two different conformations of the focus region (conventional and extended 18S rRNA). All classes were used to perform a consensus 3D reconstruction showing the overall ribosome features. Two classes showing the same conformation were combined (31,644 particles) to obtain the final map. No further refinement was conducted to avoid overfitting of the 40S beak region due to its small size.

For the Ribo$^{Rad6IP–XL}$ dataset, 2,638 aligned micrographs were imported into cryoSPARC. CTF estimation was conducted with CTFFIND4.1. A total of 1,514 micrographs were selected based on the CTF maximum resolution using a cutoff of 4.5 Å, from which 105,705 particles were selected using a blob picking job. After 2D classification, a total of 31,670 particles were selected and subjected to Ab-initio reconstruction. Final homogeneous refinement resulted in a 4.4 Å resolution map.

Molecular modeling—The coordinates for Rad6 were taken from the crystal structure of Rad6 with ubiquitin (PDB: 4R62) (Kumar et al., 2015). Ubiquitin was removed from the structure and the mutant C88K was reverted to wild type C88 by replacing the sidechain from the Dunbrack Rotamer Library (Shapovalov and Dunbrack, 2011). The coordinates for the receptor ribosome were taken from a cryo-EM reconstruction of the 80S ribosome in complex with mRNA, tRNA, and eEF2 (PDB: 6GQ1)(Pellegrino et al., 2018). Missing sidechains were built in with the Dunbrack Rotamer Library. Receptor sites on eS12 along with neighboring proteins, were isolated from the 80S ribosome prior to docking to limit search space. Rad6 was then docked to each receptor site using ClusPro 2.0 (Kozakov et al., 2017).

On each receptor site we added attraction benefits to the putative ubiquitinated lysine residues (Back et al., 2018); no restraints were added that specifically promote Rad6 C88 to interact with these lysine residues. To discriminate between the top ten scoring predictions from ClusPro 2.0 (Lensink et al., 2020), we further considered whether Rad6 C88 is proximal to the putative ubiquitinated lysine to promote catalysis.

Mass spectrometry analysis

Sample preparation: Yeast cells were cultured to mid-log phase into synthetic SILAC media supplemented with light or heavy lysine isotopes (L-Lys8 ^{13}C, ^{15}N; Cambridge Isotopes). Cells were grown for at least 10 generations in SILAC medium before being treated with 0.6 mM H_2O_2 for 30 min at 30°C. *Rad6 immunoprecipitation*: Rad6-HA (light, GMS483) and Rad6^{C88S}-HA (heavy, GMS493) cells were disrupted under denaturing conditions in standard buffer containing 8M urea and 5 mM EDTA. Urea was diluted to 1M prior to anti-HA immunoprecipitation (2 h at 4°C) and beads were washed for 5 times in 50 mM ammonium bicarbonate pH 8.0. Samples were eluted by 30 min incubation with 15 mM DTT, digested overnight with Trypsin/Lys-C (1:20 w/w, Promega), desalted using C18 Hypersep Spin Column (Thermo), and resuspended in 2% acetonitrile (MeCN), 0.1% formic acid. *Protein expression changes* (*rad6* /WT): WT (GMS280) was grown under SILAC light condition and *rad6* (GMS494) under heavy. Cell lysis was performed as above following trypsin digestion and C18 clean up. Biological triplicates were run combining equal protein amounts per strain from untreated and H_2O_2-treated conditions.

Data collection & analysis: Up to 1 μg of digests were analyzed using a nanoACQUITY UPLC system (Waters) coupled to a Fusion Lumos high-resolution accurate mass tandem mass spectrometer (ThermoFisher Scientific) via a nano-electrospray flex ion source. Briefly, peptides were trapped on a Symmetry C18 180 μm × 20 mm column (5 μL/min at 0.1% MeCN) followed by an analytical separation using a 1.7-μm ACQUITY UPLC HSS T3 C18 75 μm × 250 mm column (Waters) with a 90-min gradient of 5–30% MeCN with 0.1% formic acid at a flow rate of 400 nL/min and column temperature of 55°C. Data collection on the Fusion Lumos MS was performed in data-dependent acquisition (DDA) mode with a 120,000-resolution (at *m/z* 200) full MS scan from 375-1500 *m/z* with a target automatic gain control (AGC) value of 4×10^5 ions and maximum IT of 50 ms. Peptides were selected for data-dependent MS/MS using charge state filtering, monoisotopic precursor selection, and a dynamic exclusion of 20 s. MS/MS was performed using higher energy C-Trap dissociation with a collision energy of $30 \pm 5\%$ with detection in the ion trap using rapid scanning, an AGC target of 1×10^4 and maximum IT of 100 ms. A time-dependent (2 s) method was used. The RAW data files were processed using MaxQuant to identify and quantify protein and peptide abundance. The spectra were matched against the yeast *S. cerevisiae* Uniprot database. Protein identification was performed using 10 ppm tolerance with a posterior global FDR of 1% based on the reverse sequence of the yeast FASTA file. Up to two missed trypsin cleavages were allowed, and oxidation of methionine and N-terminal acetylation were searched as variable post-translational modification while cysteine carbamidomethylation was searched as fixed.

GFP expression determination—Indicated strains were grown in SD-Ura medium to mid-log phase. At OD_{600} 0.3–0.4, cells were pelleted and resuspended in SD-Ura-Met medium to induce expression of GFP under control of the Met25 promoter. After one hour of growth in Met-deficient medium, the cultures were incubated in the presence or absence of 0.6mM H_2O_2. At the indicated time points, cells were collected by centrifugation, washed, and resuspended in PBS for determination of OD_{600} and fluorescence. Data were normalized to the relative fluorescence unit (RFU) of GFP per OD_{600}.

Quantitative RT-PCR—Total RNA from yeast cells grown into SD-Trp-Leu to mid-log phase was isolated with YeaStar RNA Kit (Zymo Research R1002). RNA was treated with 0.02 units/μL DNase I (NEB M0303) for 10 min at 37°C, purified with RNA clean up kit (NEB T2050), and cDNA was generated with SuperScript III Reverse Transcriptase (Thermo Scientific, 18,080,044) from 2-3 μg of RNA using oligo(dT) (Invitrogen, 18,418,012) as primer. Quantitative RT-PCR was performed with 20 ng cDNA in a LightCycler instrument (Roche) using FastStart Essential DNA Green Master (Roche 06,402,712,001). Primers for quantitative RT-PCR are listed in the Key resources table. The relative transcript abundance was normalized to the expression levels of the *TAF10* gene. The relative fold change was obtained by   Ct method (Livak and Schmittgen, 2001). Abundance was determined using three biological replicates.

Flow cytometry—Wild-type and *rad6Δ* strains were grown to mid-log phase and 500 μL of untreated and H_2O_2-treated cells were fixed in 70% ethanol overnight at 4°C. Cells were centrifuged and incubated with 40 μg/mL RNAse A (ThermoFisher EN0531) in 50 mM Na-citrate buffer overnight at 50°C, followed by incubation with 100 μg/mL proteinase K (NEB P8107) overnight at 50°C. Cells were sonicated for 5 s and DNA stain SYTOX Green (Invitrogen S7020) at 2 μM was added to the cells before analysis in a BD FACSCanto cell sorter. Data analysis was performed using FlowJo software.

QUANTIFICATION AND STATISTICAL ANALYSIS

iBright Analysis Software was used for Western blot quantification. Band intensity was measured from images captured in g2i format from three biological replicates. Analyses used Students t-test and further details were provided in the figure legends. Differences were considered statistically significant at a value of $p < 0.05$. Proteomics statistical analyses, data transformation, and filtering were performed in Perseus (Tyanova et al., 2016). For SILAC-based analyses, two-sample Student's t-tests were performed with permutation-based FDR set at 0.05.

Supplementary Material

Refer to Web version on PubMed Central for supplementary material.

ACKNOWLEDGMENTS

REFERENCES

Back S, Gorman AW, Vogel C, and Silva GM (2018). Site-specific K63 ubiquitinomics provides insights into translation regulation under stress. J. Proteome. Res 18, 309–318. 10.1021/acs.jproteome.8b00623. [PubMed: 30489083]

Brandes N, Schmitt S, and Jakob U (2009). Thiol-based redox switches in eukaryotic proteins. Antioxid. Redox Signal 11, 997–1014. 10.1089/ARS.2008.2285. [PubMed: 18999917]

Bruinsma CF, Savelberg SMC, Kool MJ, Jolfaei MA, Van Woerden GM, Baarends WM, and Elgersma Y (2016). An essential role for UBE2A/HR6A in learning and memory and mGLUR-dependent long-term depression. Hum. Mol. Genet 25, 1–8. 10.1093/hmg/ddv436. [PubMed: 26476408]

Buetow L, and Huang DT (2016). Structural insights into the catalysis and regulation of E3 ubiquitin ligases. Nat. Rev. Mol. Cell. Biol 17, 626–642. 10.1038/nrm.2016.91. [PubMed: 27485899]

Chung HS, Wang SB, Venkatraman V, Murray CI, and Van Eyk JE (2013). Cysteine oxidative posttranslational modifications: emerging regulation in the cardiovascular system. Circ. Res 112, 382–392. 10.1161/CIRCRESAHA.112.268680. [PubMed: 23329793]

Cox J, and Mann M (2008). MaxQuant enables high peptide identification rates, individualized p.p.b.-range mass accuracies and proteome-wide protein quantification. Nat. Biotechnol 26, 1367–1372. 10.1038/nbt.1511. [PubMed: 19029910]

Czeschik JC, Bauer P, Buiting K, Dufke C, Guillen-Navarro E, Johnson DS, Koehler U, Lopez-Gonzalez V, Ludecke HJ, Male A, et al. (2013). X-linked intellectual disability type Nascimento is a clinically distinct, probably underdiagnosed entity. Orphanet J. Rare. Dis 8, 146. 10.1186/1750-1172-8-146. [PubMed: 24053514]

de Oliveira JF, do Prado PFV, da Costa SS, Sforca ML, Canateli C, Ranzani AT, Maschietto M, de Oliveira PSL, Otto PA, Klevit RE, et al. (2019). Mechanistic insights revealed by a UBE2A mutation linked to intellectual disability. Nat. Chem. Biol 15, 62–70. 10.1038/s41589-018-0177-2. [PubMed: 30531907]

Dohmen RJ, Madura K, Bartel B, and Varshavsky A (1991). The N-end rule is mediated by the UBC2(RAD6) ubiquitin-conjugating enzyme. Proc. Natl. Acad. Sci. U S A 88, 7351–7355. 10.1073/pnas.88.16.7351. [PubMed: 1651502]

Doris KS, Rumsby EL, and Morgan BA (2012). Oxidative stress responses involve oxidation of a conserved ubiquitin pathway enzyme. Mol. Cell. Biol 32, 4472–4481. 10.1128/MCB.00559-12. [PubMed: 22949505]

Dougherty SE, Maduka AO, Inada T, and Silva GM (2020). Expanding role of ubiquitin in translational control. Int. J. Mol. Sci 21, 1151. 10.3390/ijms21031151.

Emsley P, and Cowtan K (2004). Coot: model-building tools for molecular graphics. Acta Crystallogr. D Biol. Crystallogr 60, 2126–2132. 10.1107/S0907444904019158. [PubMed: 15572765]

Finley D, Ulrich HD, Sommer T, and Kaiser P (2012). The ubiquitin-proteasome system of Saccharomyces cerevisiae. Genetics 192, 319–360. 10.1534/genetics.112.140467. [PubMed: 23028185]

Flis J, Holm M, Rundlet EJ, Loerke J, Hilal T, Dabrowski M, Burger J, Mielke T, Blanchard SC, Spahn CMT, and Budkevich TV (2018). tRNA translocation by the eukaryotic 80S ribosome and the impact of GTP hydrolysis. Cell Rep. 25, 2676–2688.e7. 10.1016/j.celrep.2018.11.040. [PubMed: 30517857]

Gamerdinger M, Kobayashi K, Wallisch A, Kreft SG, Sailer C, Schlomer R, Sachs N, Jomaa A, Stengel F, Ban N, and Deuerling E (2019). Early scanning of nascent polypeptides inside the ribosomal tunnel by NAC. Mol. Cell 75, 996–1006.e8. 10.1016/j.molcel.2019.06.030. [PubMed: 31377116]

Grant CM (2011). Regulation of translation by hydrogen peroxide. Antioxid. Redox Signal 15, 191–203. 10.1089/ars.2010.3699. [PubMed: 21126188]

Grant T, Rohou A, and Grigorieff N (2018). cisTEM, user-friendly software for single-particle image processing. eLife 7, e35383. 10.7554/eLife.35383. [PubMed: 29513216]

Haddad DM, Vilain S, Vos M, Esposito G, Matta S, Kalscheuer VM, Craessaerts K, Leyssen M, Nascimento RM, Vianna-Morgante AM, et al. (2013). Mutations in the intellectual disability gene Ube2a cause neuronal dysfunction and impair parkin-dependent mitophagy. Mol. Cell 50, 831–843. 10.1016/j.molcel.2013.04.012. [PubMed: 23685073]

Hanna J, Leggett DS, and Finley D (2003). Ubiquitin depletion as a key mediator of toxicity by translational inhibitors. Mol. Cell. Biol 23, 9251–9261. 10.1128/mcb.23.24.9251-9261.2003. [PubMed: 14645527]

Hodge CD, Spyracopoulos L, and Glover JNM (2016). Ubc13: the Lys63 ubiquitin chain building machine. Oncotarget 7, 64471–64504. 10.18632/oncotarget.10948. [PubMed: 27486774]

Hoege C, Pfander B, Moldovan GL, Pyrowolakis G, and Jentsch S (2002). RAD6-dependent DNA repair is linked to modification of PCNA by ubiquitin and SUMO. Nature 419, 135–141. 10.1038/nature00991. [PubMed: 12226657]

Holcik M, and Sonenberg N (2005). Translational control in stress and apoptosis. Nat. Rev. Mol. Cell. Biol 6, 318–327. 10.1038/nrm1618. [PubMed: 15803138]

Inada T (2013). Quality control systems for aberrant mRNAs induced by aberrant translation elongation and termination. Biochim. Biophys. Acta 1829, 634–642. 10.1016/j.bbagrm.2013.02.004. [PubMed: 23416749]

Joazeiro CAP (2019). Mechanisms and functions of ribosome-associated protein quality control. Nat. Rev. Mol. Cell. Biol 20, 368–383. 10.1038/s41580-019-0118-2. [PubMed: 30940912]

Kitanovic A, Walther T, Loret MO, Holzwarth J, Kitanovic I, Bonowski F, Bui NV, Francois JM, and WÃ¶lfl S. (2009). Metabolic response to MMS-mediated DNA damage in Saccharomyces cerevisiae is dependent on the glucose concentration in the medium. FEMS Yeast Res. 9, 535–551. 10.1111/j.1567-1364.2009.00505.x. [PubMed: 19341380]

Koken M, Reynolds P, Bootsma D, Hoeijmakers J, Prakash S, and Prakash L (1991a). Dhr6, a Drosophila homolog of the yeast DNA-repair gene RAD6. Proc. Natl. Acad. Sci. U S A 88, 3832–3836. 10.1073/pnas.88.9.3832. [PubMed: 1902572]

Koken MH, Reynolds P, Jaspers-Dekker I, Prakash L, Prakash S, Bootsma D, and Hoeijmakers JH (1991b). Structural and functional conservation of two human homologs of the yeast DNA repair gene RAD6. Proc. Natl. Acad. Sci. U S A 88, 8865–8869. 10.1073/pnas.88.20.8865. [PubMed: 1717990]

Kozakov D, Hall DR, Xia B, Porter KA, Padhorny D, Yueh C, Beglov D, and Vajda S (2017). The ClusPro web server for protein-protein docking. Nat. Protoc 12, 255–278. 10.1038/nprot.2016.169. [PubMed: 28079879]

Kumar P, Magala P, Geiger-Schuller KR, Majumdar A, Tolman JR, and Wolberger C (2015). Role of a non-canonical surface of Rad6 in ubiquitin conjugating activity. Nucleic Acids Res. 43, 9039–9050. 10.1093/nar/gkv845. [PubMed: 26286193]

Lee JG, Baek K, Soetandyo N, and Ye Y (2013). Reversible inactivation of deubiquitinases by reactive oxygen species in vitro and in cells. Nat. Commun 4, 1568. 10.1038/ncomms2532. [PubMed: 23463011]

Lensink MF, Nadzirin N, Velankar S, and Wodak SJ (2020). Modeling protein-protein, protein-peptide, and protein-oligosaccharide complexes: CAPRI 7th edition. Proteins 88, 916–938. 10.1002/prot.25870. [PubMed: 31886916]

Liu C, Apodaca J, Davis LE, and Rao H (2007). Proteasome inhibition in wild-type yeast Saccharomyces cerevisiae cells. Biotechniques 42, 158. 10.2144/000112389. [PubMed: 17373478]

Livak KJ, and Schmittgen TD (2001). Analysis of relative gene expression data using real-time quantitative PCR and the 2– CT method. Methods 25, 402–408. 10.1006/meth.2001.1262. [PubMed: 11846609]

Magistroni V, Mauri M, D'Aliberti D, Mezzatesta C, Crespiatico I, Nava M, Fontana D, Sharma N, Parker W, Schreiber A, et al. (2019). De novo UBE2A mutations are recurrently acquired during chronic myeloid leukemia progression and interfere with myeloid differentiation pathways. Haematologica 104, 1789–1797. 10.3324/haematol.2017.179937. [PubMed: 30819912]

Manohar S, Jacob S, Wang JC, Wiechecki KA, Koh HW, Simoes V, Choi H, Vogel C, and Silva GM (2019). Polyubiquitin chains linked by lysine residue 48 (K48) selectively target oxidized proteins in vivo. Antioxid. Redox Signal 31, 1133–1149. 10.1089/ars.2019.7826. [PubMed: 31482721]

Mastronarde DN (2005). Automated electron microscope tomography using robust prediction of specimen movements. J. Struct. Biol 152, 36–51. 10.1016/j.jsb.2005.07.007. [PubMed: 16182563]

Masuda Y, Suzuki M, Kawai H, Hishiki A, Hashimoto H, Masutani C, Hishida T, Suzuki F, and Kamiya K (2012). En bloc transfer of polyubiquitin chains to PCNA in vitro is mediated by two different human E2-E3 pairs. Nucleic Acids Res. 40, 10394–10407. 10.1093/nar/gks763. [PubMed: 22904075]

Matsuo Y, Ikeuchi K, Saeki Y, Iwasaki S, Schmidt C, Udagawa T, Sato F, Tsuchiya H, Becker T, Tanaka K, et al. (2017). Ubiquitination of stalled ribosome triggers ribosome-associated quality control. Nat. Commun 8, 159. 10.1038/s41467-017-00188-1. [PubMed: 28757607]

Nascimento RM, Otto PA, de Brouwer AP, and Vianna-Morgante AM (2006). UBE2A, which encodes a ubiquitin-conjugating enzyme, is mutated in a novel X-linked mental retardation syndrome. Am. J. Hum. Genet 79, 549–555. 10.1086/507047. [PubMed: 16909393]

Netto LES, de Oliveira MA, Monteiro G, Demasi APD, Cussiol JRR, Discola KF, Demasi M, Silva GM, Alves SV, Faria VG, and Horta BB (2007). Reactive cysteine in proteins: protein folding, antioxidant defense, redox signaling and more. Comp. Biochem. Physiol. C Toxicol. Pharmacol 146, 180–193. 10.1016/j.cbpc.2006.07.014. [PubMed: 17045551]

Ong SE, Blagoev B, Kratchmarova I, Kristensen DB, Steen H, Pandey A, and Mann M (2002). Stable isotope labeling by amino acids in cell culture, SILAC, as a simple and accurate approach to expression proteomics. Mol. Cell. Proteomics 1, 376–386. 10.1074/mcp.m200025-mcp200. [PubMed: 12118079]

Pellegrino S, Demeshkina N, Mancera-Martinez E, Melnikov S, Simonetti A, Myasnikov A, Yusupov M, Yusupova G, and Hashem Y (2018). Structural insights into the role of diphthamide on elongation factor 2 in mRNA reading-frame maintenance. J. Mol. Biol 430, 2677–2687. 10.1016/j.jmb.2018.06.006. [PubMed: 29886014]

Pochopien AA, Beckert B, Kasvandik S, Berninghausen O, Beckmann R, Tenson T, and Wilson DN (2021). Structure of Gcn1 bound to stalled and colliding 80S ribosomes. Proc. Natl. Acad. Sci. U S A 118, e2022756118. 10.1073/pnas.2022756118. [PubMed: 33790014]

Punjani A, Rubinstein JL, Fleet DJ, and Brubaker MA (2017). cryoSPARC: algorithms for rapid unsupervised cryo-EM structure determination. Nat. Methods 14, 290–296. 10.1038/nmeth.4169. [PubMed: 28165473]

Raboy B, and Kulka RG (1994). Role of the C-terminus of Saccharomyces cerevisiae ubiquitin-conjugating enzyme (Rad6) in substrate and ubiquitin-protein-ligase (E3-R) interactions. Eur. J. Biochem 221, 247–251. 10.1111/j.1432-1033.1994.tb18735.x. [PubMed: 8168512]

Rohou A, and Grigorieff N (2015). CTFFIND4: fast and accurate defocus estimation from electron micrographs. J. Struct. Biol 192, 216–221. 10.1016/j.jsb.2015.08.008. [PubMed: 26278980]

Ryan OW, Poddar S, and Cate JH (2016). CRISPR-Cas9 genome engineering in Saccharomyces cerevisiae cells. Cold. Spring. Harb. Protoc 2016, pdb.prot086827. 10.1101/pdb.prot086827.

Scheres SH (2012). RELION: implementation of a Bayesian approach to cryo-EM structure determination. J. Struct. Biol 180, 519–530. 10.1016/j.jsb.2012.09.006. [PubMed: 23000701]

Shapovalov MV, and Dunbrack RL Jr. (2011). A smoothed backbone-dependent rotamer library for proteins derived from adaptive kernel density estimates and regressions. Structure 19, 844–858. 10.1016/j.str.2011.03.019. [PubMed: 21645855]

Silva GM, Finley D, and Vogel C (2015). K63 polyubiquitination is a new modulator of the oxidative stress response. Nat. Struct. Mol. Biol 22, 116–123. 10.1038/nsmb.2955. [PubMed: 25622294]

Snyder NA, and Silva GM (2021). Deubiquitinating enzymes (DUBs): regulation, homeostasis, and oxidative stress response. J. Biol. Chem 297, 101077. 10.1016/j.jbc.2021.101077. [PubMed: 34391779]

Spence J, Gali RR, Dittmar G, Sherman F, Karin M, and Finley D (2000). Cell cycle-regulated modification of the ribosome by a variant multiubiquitin chain. Cell 102, 67–76. 10.1016/s0092-8674(00)00011-8. [PubMed: 10929714]

Stewart MD, Ritterhoff T, Klevit RE, and Brzovic PS (2016). E2 enzymes: more than just middle men. Cell Res. 26, 423–440. 10.1038/cr.2016.35. [PubMed: 27002219]

Sugiyama T, Li S, Kato M, Ikeuchi K, Ichimura A, Matsuo Y, and Inada T (2019). Sequential ubiquitination of ribosomal protein uS3 triggers the degradation of non-functional 18S rRNA. Cell Rep. 26, 3400–3415.e7. 10.1016/j.celrep.2019.02.067. [PubMed: 30893611]

Sung P, Prakash S, and Prakash L (1988). The RAD6 protein of Saccharomyces cerevisiae polyubiquitinates histones, and its acidic domain mediates this activity. Genes Dev. 2, 1476–1485. 10.1101/gad.2.11.1476. [PubMed: 2850263]

Tokgoz Z, Siepmann TJ, Streich F Jr., Kumar B, Klein JM, and Haas AL (2012). E1-E2 interactions in ubiquitin and Nedd8 ligation pathways. J. Biol. Chem 287, 311–321.10.1074/jbc.M111.294975. [PubMed: 22069333]

Topf U, Suppanz I, Samluk L, Wrobel L, Boser A, Sakowska P, Knapp B , Pietrzyk MK, Chacinska A, and Warscheid B (2018). Quantitative proteomics identifies redox switches for global translation modulation by mitochondrially produced reactive oxygen species. Nat. Commun 9, 324. 10.1038/s41467-017-02694-8. [PubMed: 29358734]

Tyanova S, Temu T, Sinitcyn P, Carlson A, Hein MY, Geiger T, Mann M, and Cox J (2016). The Perseus computational platform for comprehensive analysis of (prote)omics data. Nat. Methods 13, 731–740. 10.1038/nmeth.3901. [PubMed: 27348712]

Vogel C, Silva GM, and Marcotte EM (2011). Protein expression regulation under oxidative stress. Mol. Cell. Proteomics, M111.009217. 10.1074/mcp.m111.009217.

Williams KM, Qie S, Atkison JH, Salazar-Arango S, Alan Diehl J, and Olsen SK (2019). Structural insights into E1 recognition and the ubiquitin-conjugating activity of the E2 enzyme Cdc34. Nat. Commun 10, 3296. 10.1038/s41467-019-11061-8. [PubMed: 31341161]

Worthylake DK, Prakash S, Prakash L, and Hill CP (1998). Crystal structure of the Saccharomyces cerevisiae ubiquitin-conjugating enzyme Rad6 at 2.6 A resolution. J. Biol. Chem 273, 6271–6276. 10.1074/jbc.273.11.6271. [PubMed: 9497353]

Wu L, Zee BM, Wang Y, Garcia BA, and Dou Y (2011). The RING finger protein MSL2 in the MOF complex is an E3 ubiquitin ligase for H2B K34 and is involved in crosstalk with H3 K4 and K79 methylation. Mol. Cell 43, 132–144. 10.1016/j.molcel.2011.05.015. [PubMed: 21726816]

Yang Y, Kitagaki J, Dai RM, Tsai YC, Lorick KL, Ludwig RL, Pierre SA, Jensen JP, Davydov IV, Oberoi P, et al. (2007). Inhibitors of ubiquitin-activating enzyme (E1), a new class of potential cancer therapeutics. Cancer Res. 67, 9472–9481, [pii]. 10.1158/0008-5472.CAN-07-0568. [PubMed: 17909057]

Zhou Y, Kastritis PL, Dougherty SE, Bouvette J, Hsu AL, Burbaum L, Mosalaganti S, Pfeffer S, Hagen WJH, Forster F, et al. (2020a). Structural impact of K63 ubiquitin on yeast translocating ribosomes under oxidative stress. Proc. Natl. Acad. Sci. U S A 117, 22157–22166. 10.1073/pnas.2005301117. [PubMed: 32855298]

Zhou Y, Moscovich A, Bendory T, and Bartesaghi A (2020b). Unsupervised particle sorting for high-resolution single-particle cryo-EM. Inverse Probl. 36, 044002. 10.1088/1361-6420/ab5ec8.

Zivanov J, Nakane T, Forsberg BO, Kimanius D, Hagen WJ, Lindahl E, and Scheres SH (2018). New tools for automated high-resolution cryo-EM structure determination in RELION-3. eLife 7, e42166. 10.7554/eLife.42166. [PubMed: 30412051]

Highlights

- The E2 Rad6 mediates K63-linked ubiquitination of ribosomes under stress

- Rad6 forms a reversible redox disulfide with Uba1 (E1)

- Rad6-Uba1 complex controls K63 ubiquitination in a negative feedback mechanism

- Rad6 is critical for the stress response through control of translation
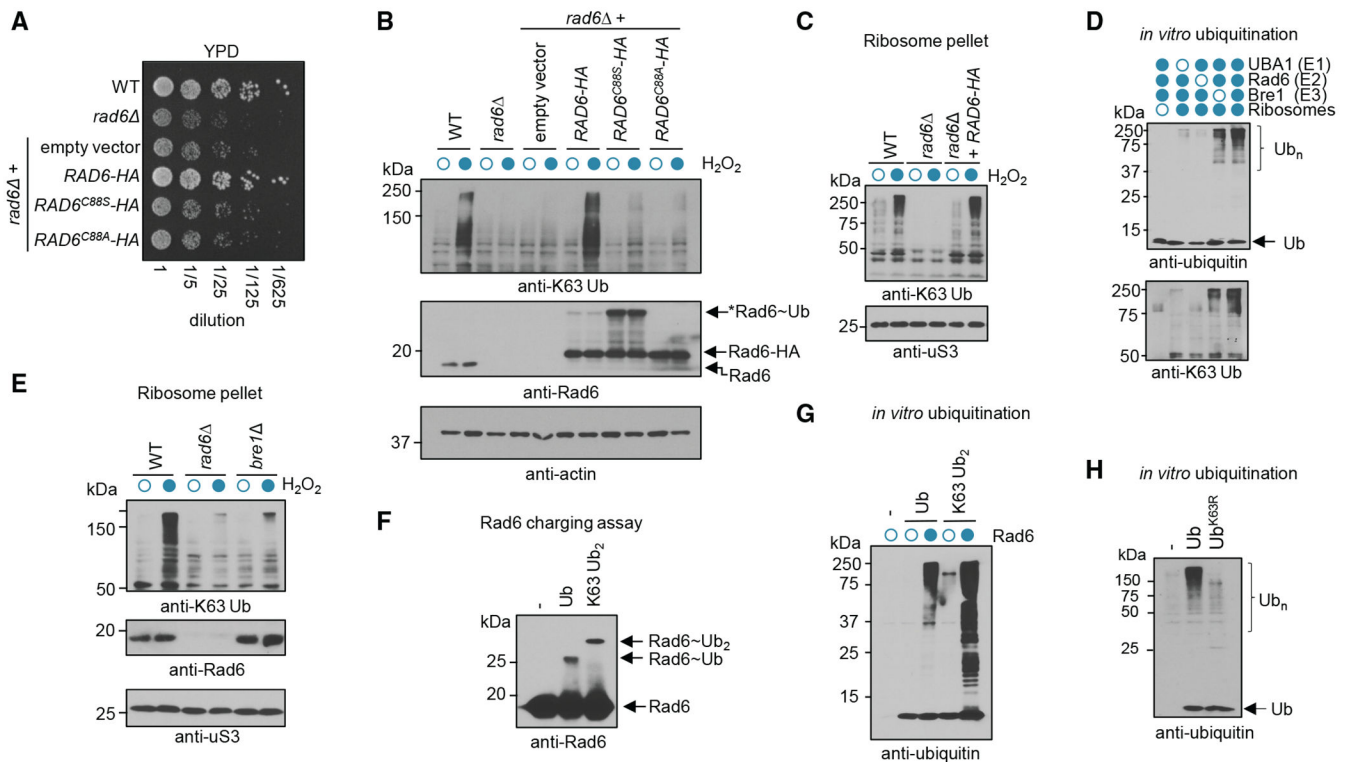
Figure 1. Rad6 is responsible for K63 ubiquitination of ribosomes

(A–C) Episomal expression of HA-tagged Rad6 reverts *rad6Δ* growth defect (A) and supports the accumulation of K63 ubiquitin chains under 0.6 mM H_2O_2 as visualized by immunoblotting whole-cell lysate (B) or isolated ribosomes (C). *Rad6 bound to ubiquitin. Anti-actin was used as loading control for whole-cell lysate, and anti-uS3 was used as ribosomal loading control.

(D) Immunoblot from *in vitro* ubiquitination assay of ribosomes isolated from *rad6Δ bre1Δ* cells in the presence of recombinant Rad6 ubiquitination system as described in the STAR Methods. All lanes contain wild-type ubiquitin, ATP, energy-generation system, and DTT.

(E) Accumulation of K63-linked ubiquitin chains in yeast cells depend on *RAD6* and *BRE1*. Immunoblot anti-K63 ubiquitin chains from ribosomes isolated from cells treated in the presence or absence of 0.6 mM H_2O_2 for 30 min. Anti-uS3 was used as ribosomal loading control.

(F) Immunoblot of *in vitro* reactions shows Rad6 charged with ubiquitin monomer (Ub) and K63-linked di-ubiquitin (K63 Ub_2). All lanes contain Rad6, E1, and ATP.

(G) Immunoblot of *in vitro* ubiquitination assay of ribosomes with wild-type ubiquitin monomer (Ub) or K63-linked di-ubiquitin chains (K63 Ub_2). All lanes contain E1, Bre1, ATP, energy-generation system, DTT, and ribosomes from *rad6Δ bre1Δ* strain.

(H) Immunoblot of *in vitro* ubiquitination assay of ribosomes with wild-type (WT) ubiquitin monomer or K63R mutant ubiquitin (K63R). All lanes contain E1, Bre1, ATP, energy-generation system, DTT, and ribosomes from *rad6Δ bre1Δ* strain.
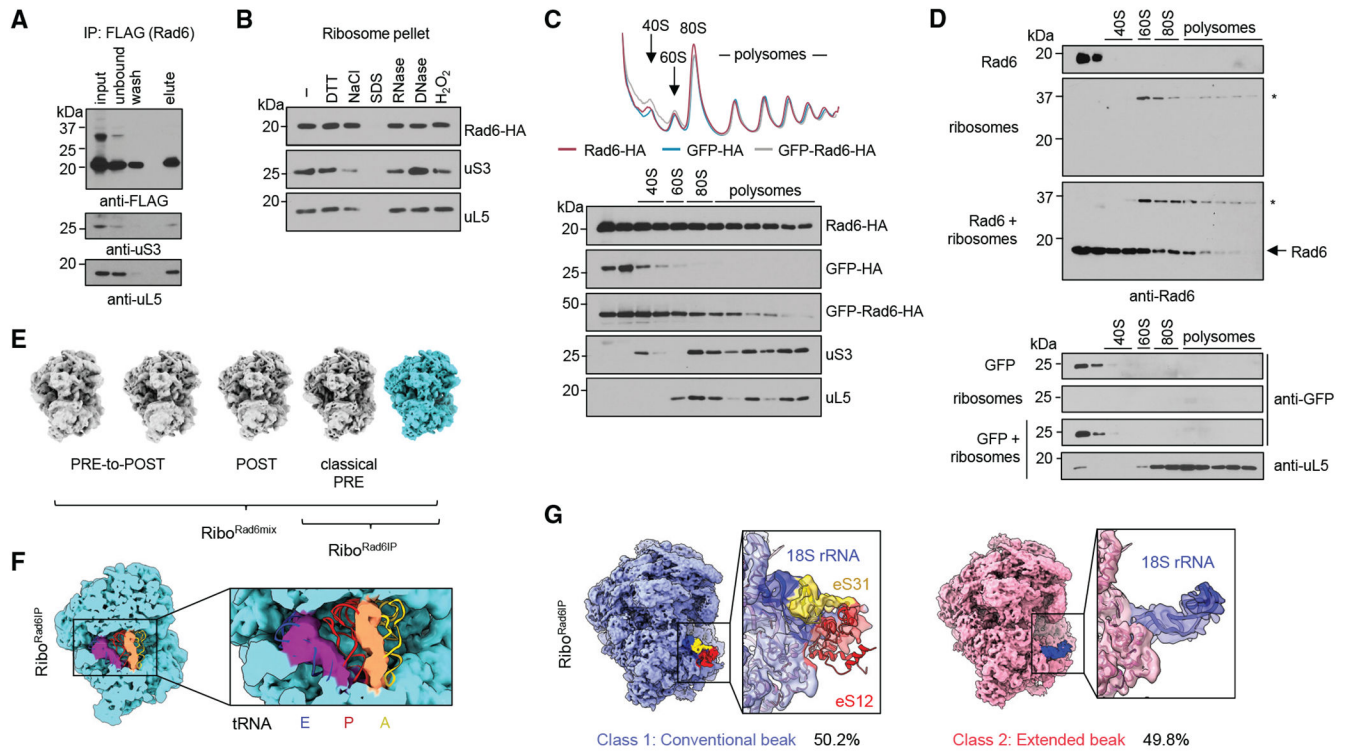
Figure 2. Rad6 co-sediments with elongating ribosomes

(A) Immunoblot of co-immunoprecipitation (coIP) of Rad6-FLAG with ribosomal proteins uS3 and uL5.

(B) Rad6 presence on the ribosome pellet is independent of cellular lysate incubation with 10 mM DTT, 1 M NaCl, 1 mM H_2O_2, and DNAse (0.1 U/μg protein) and RNAse I (100 U/μg protein). 1% SDS was used to disrupt molecular interactions. Anti-uS3 and -uL5 were used as loading control for proteins from the 40S and 60S ribosome subunits, respectively.

(C) Sucrose density sedimentation analysis and anti-HA immunoblot of lysates from cells expressing Rad6-HA, GFP-HA, or GFP-Rad6-HA constructs. Anti-uS3 and -uL5 were used as markers for the 40S and 60S ribosome subunits, respectively.

(D) Purified Rad6, but not GFP, relocalizes to the polysomal fraction after incubation with ribosomes for 10 min at room temperature followed by sucrose density-sedimentation separation. Ribosomes were isolated from *rad6 bre1* strain. Anti-uL5 was used as a marker for the 60S ribosome subunit. *Anti-Rad6 antibody unspecific band.

(E) 3D classification of ribosomes incubated with purified Rad6 (Ribo^Rad6mix) and ribosomes co-immunoprecipitated with FLAG-tagged Rad6 (Ribo^Rad6IP). Ribosomes were observed in the pre-translocation (PRE), post-translocation (POST), and transition (PRE-to-POST) states.

(F) Structural detail of Ribo^Rad6IP at the pre-translocation stage with tRNAs in hybrid A/P and P/E positions. Rigid fit of the tRNAs was performed using coordinates from the 80S ribosome (PDB: 6GZ5) (Flis et al., 2018).

(G) Focused classification of Ribo^Rad6IP shows two classes with distinct conformations for the 40S beak and ribosomal proteins eS12 and eS31. The extended beak rRNA model was built using COOT (Emsley and Cowtan, 2004).
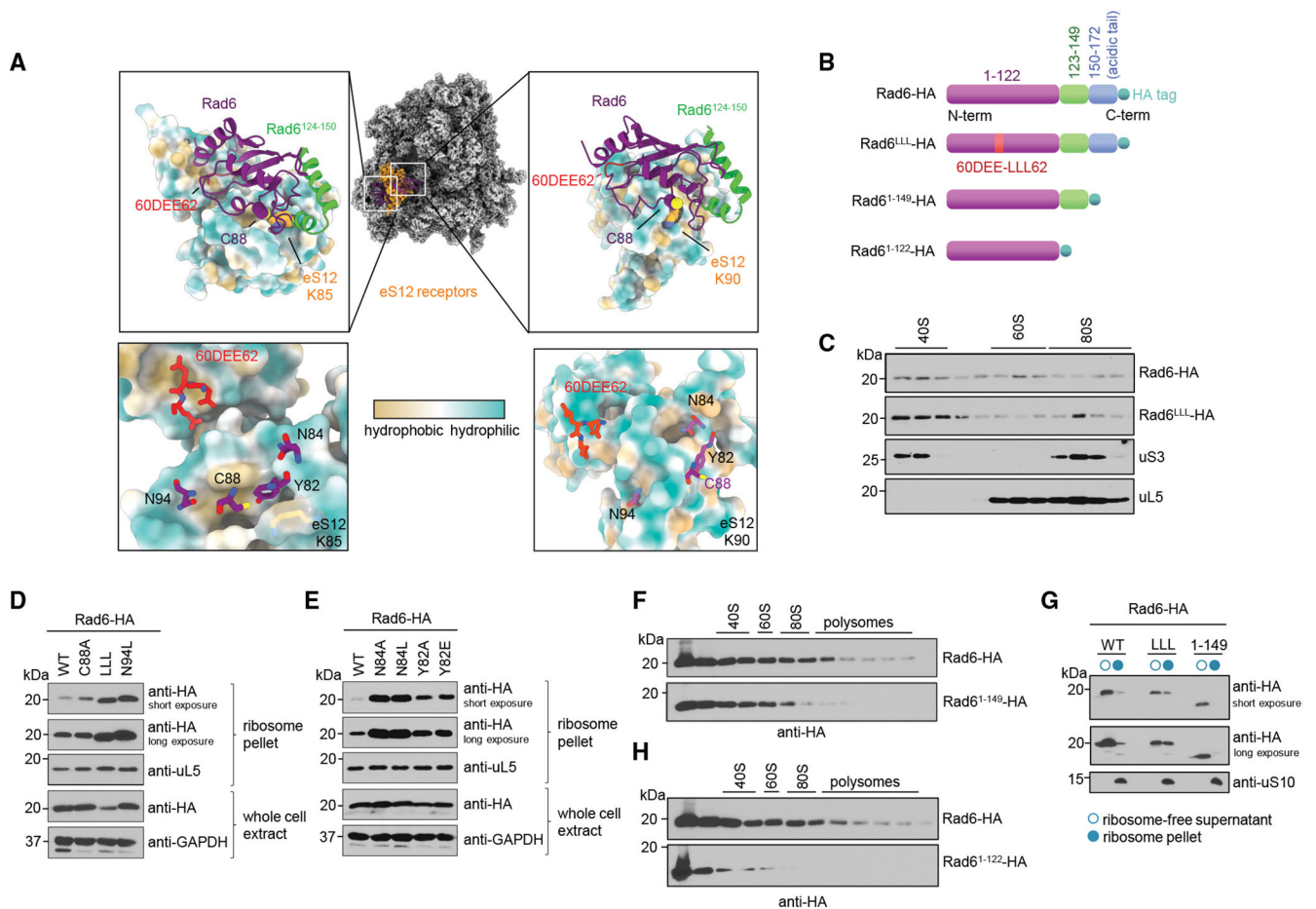
Figure 3. Hydrophobic surfaces impact Rad6's association to ribosomes

(A) Molecular docking predicts the binding poses of Rad6 on the ribosome for two ubiquitination sites on eS12 (K85 and K90). In the blowouts, the ribosome receptor sites are shown as a surface and are colored tan/cyan for hydrophobic/hydrophilic residues. Details are provided for the predicted contact sites. Additional views for these interaction surfaces are present in Figure S4F.

(B) Schematic of Rad6 constructs with respective name notations. Green represents the C-terminal last alpha helix, blue represents the C-terminal acidic tail, and red represents the acid region DEE60-62.

(C) Immunoblot from sucrose density sedimentation analysis shows differential ribosomal association pattern for Rad6^{LLL} variant. Anti-uS3 and -uL5 were used as markers for the 40S and 60S ribosome subunits, respectively.

(D and E) Anti-HA (Rad6) immunoblot after sucrose cushion for Rad6 variants. Rad6^{LLL} and Rad6^{N94L} (D) and Rad6^{N84A}, Rad6^{N84L}, Rad6^{Y82A}, and Rad6^{Y82E} (E) have an increased presence in the ribosome pellet. Anti-HA (Rad6) was used to determine expression levels of Rad6 variants in the whole-cell lysate, anti-GADPH was used as loading control for whole-cell lysate, and anti-uS3 was used as ribosomal loading control.

(F) Immunoblot from sucrose density sedimentation analysis shows reduced ribosomal co-sedimentation for Rad6$^{1-149}$ variant. Same gel comparison is presented in Figure S5A.

(G) Immunoblot from supernatant (open circle) and ribosome pellet (full circle) after sucrose cushion from strains expressing Rad6$^{1-149}$ and Rad6^{LLL} variants. uS10 was used as ribosome marker.

(H) Immunoblot from sucrose density sedimentation analysis shows reduced ribosomal co-sedimentation for Rad6$^{1-122}$ variant. Same gel comparison is presented in Figure S5B.
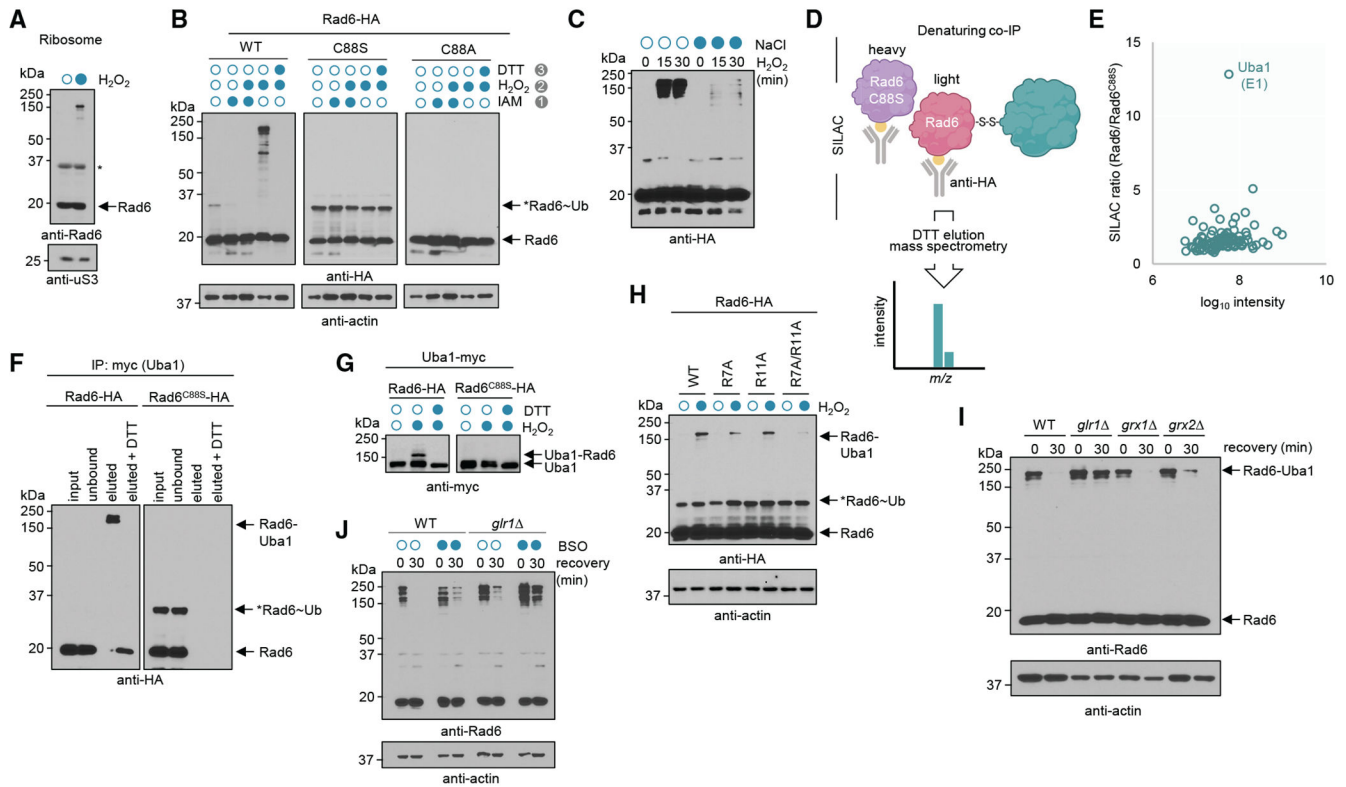
Figure 4. Rad6 is redox regulated by disulfide formation with the E1 enzyme Uba1

(A) Non-reducing immunoblot of isolated ribosomes from cells exposed to 0.6 mM H_2O_2 for 30 min reveals a Rad6-containing high-molecular-weight complex. Anti-uS3 was used as ribosomal loading control. *Anti-Rad6 antibody unspecific band.

(B) Non-reducing immunoblot of yeast cell lysate shows formation, prevention, and reduction of Rad6 high-molecular-weight complexes. Cell lysate from yeast cells expressing HA-tagged WTRad6, C88S, or C88A mutants were alkylated with 20 mM IAM, oxidized with 2 mM H_2O_2, or reduced with 15 mM DTT for 30 min at room temperature (RT) prior to immunoblot. *Rad6 bound to ubiquitin.

(C) Formation of Rad6 disulfides in yeast cell lysate is impacted by 1 M NaCl prior to 2 mM H_2O_2 treatment for the designated times.

(D) Schematic of the denaturing coIP coupled with SILAC liquid chromatography-tandem mass spectrometry (LC-MS/MS) to identify Rad6 redox partner. Created with BioRender.com.

(E) Scatterplot of MS/MS intensity and SILAC ratio of Rad6/Rad6^{C88S} under H_2O_2 stress.

(F) Immunoblot anti-HA (Rad6) of Uba1-myc coIP shows complex with Rad6-HA but not with Rad6^{C88S}, which is reduced by 15 mM DTT. *Rad6 bound to ubiquitin.

(G) Immunoblot anti-myc (Uba1) shows disulfide formation upon 0.6 mM H_2O_2 treatment for cells expressing WT Rad6 but not Rad6^{C88S}, which is reduced by 15 mM DTT.

(H) Immunoblot of Rad6 mutants (R7A, R11A, R7A/R11A) show differential formation of Rad6-Uba1 complex in cells exposed to 0.6 mM H_2O_2. *Rad6 charged with ubiquitin through thioester bond.

(I) Immunoblot anti-Rad6 shows that deletion of glutathione reductase (*GLR1*) slows down the reduction of the Rad6-Uba1 complex during stress recovery after treatment with 0.6 mM H_2O_2 for 30 min.

(J) Immunoblot anti-Rad6 shows that the reversal of Rad6-Uba1 complex is impacted by glutathione balance. Cells were grown into MPD medium (Liu et al., 2007) in the presence or absence 2.5 mM of BSO, an inhibitor of glutathione synthesis, for 3 h prior to treatment with 0.6 mM H_2O_2 for 30 min, followed by recovery from stress for 30 min.
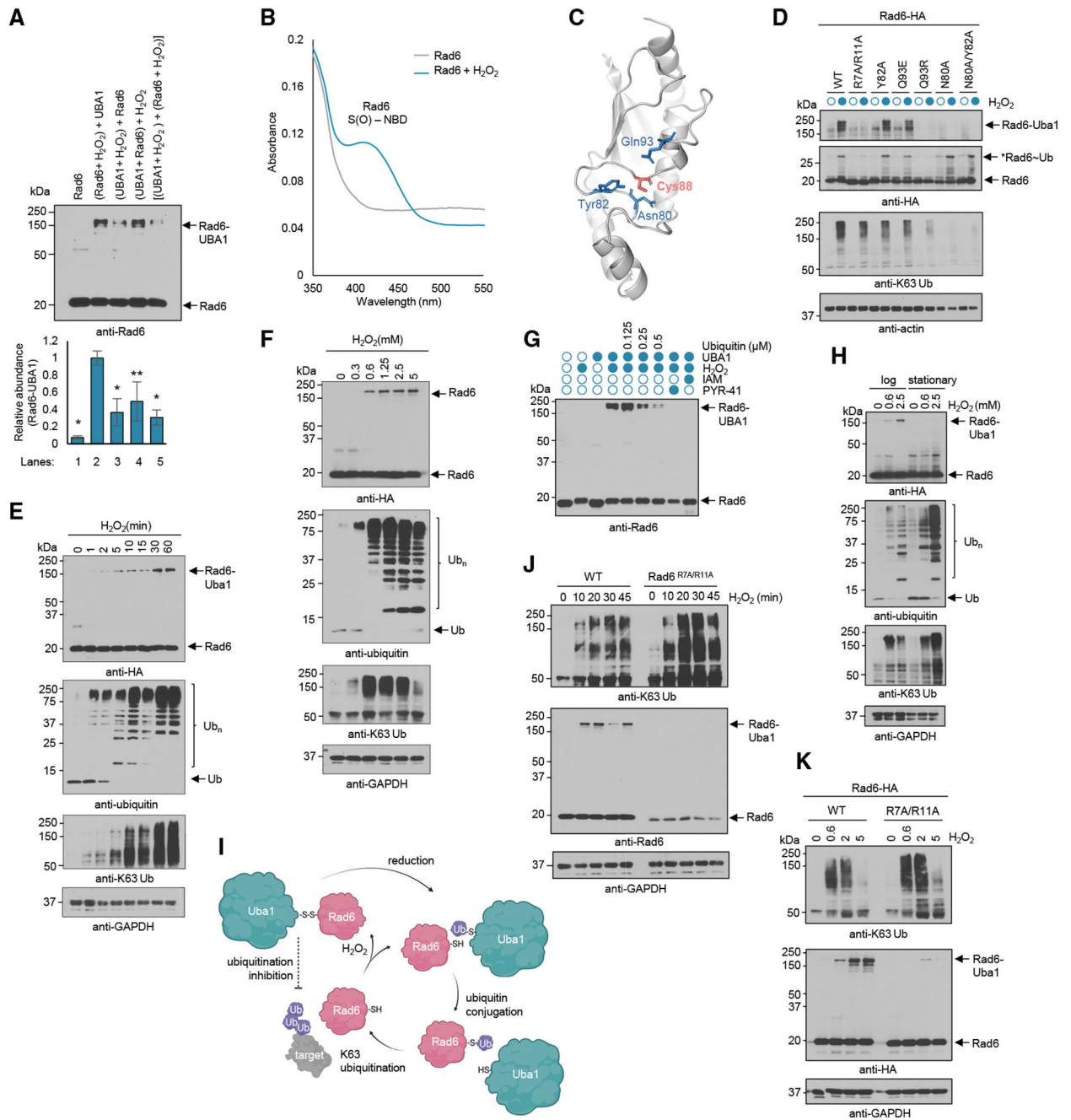
Figure 5. Formation of Rad6-Uba1 disulfide depends on free ubiquitin and controls K63 ubiquitination

(A) Representative immunoblot anti-Rad6 from *in vitro* oxidation reactions of recombinant Rad6 (100 nM) and UBA1 (100 nM) in the presence of 2 mM H_2O_2. Lane labels describe the sequential order of events and which protein was oxidized prior to mixing. Quantification was performed using iBright Analysis Software, and graph shows mean ± standard deviation for three biological replicates. Quantification of Rad6-E1 band was normalized by the amount present in lane 2 compared with the levels of DTT-reduced Rad6 for each sample. *p   0.005, **p   0.025 determined by Student's t test.

(B) Spectroscopic analysis of 75 μg of purified Rad6 treated in the presence or absence of 2 mM H_2O_2 for 30 min at RT. Samples were then incubated with 100 μM 4-chloro-7-nitrobenzofurazan (NBD) for an additional 30 min, followed by removal of excess reagent by successive cycles of washes and filtration. Rad6 sulfenic acid peak is exhibited at 420 nm.

(C) Close-up view of Rad6 active site (PDB: 1AYZ) highlighting its catalytic cysteine (pink) and vicinal residues (blue) as sticks.

(D) Immunoblots of Rad6 mutants for amino-acid residues interacting with catalytic Cys88 show differential ubiquitination and disulfide formation. Anti-actin was used as loading control. *Rad6 charged with ubiquitin through thioester bond.

(E) Immunoblots anti-Rad6, anti-K63 ubiquitin chains, and anti-ubiquitin show dynamics of Rad6-Uba1 complex and polyubiquitin chain formation as well as depletion of the pool of monomeric ubiquitin over time after cellular exposure to 0.6 mM H_2O_2. Anti-GAPDH was used as loading control.

(F) Accumulation of Rad6-Uba1 complex and depletion of the ubiquitin pool is dose dependent. Immunoblot from Rad6-HA-expressing cells subjected to increased H_2O_2 concentrations for 30 min. Anti-GAPDH was used as loading control.

(G) Immunoblot from *in vitro* incubation of yeast recombinant Rad6 (100 nM) and UBA1 (100 μM) in the presence of increased ubiquitin concentration for 30 min followed by 2 mM H_2O_2 treatment for 30 min. Proteins were also pre-incubated with the E1 inhibitor PYR-41 (75 μM) or alkylated with iodoacetamide (20 mM) for 30 min prior to exposure to H_2O_2.

(H) Yeast cells at stationary phase do not show Rad6-Uba1 disulfide formation and have high levels of K63 ubiquitin chains. Immunoblot of cells treated with indicated H_2O_2 concentrations for 30 min in mid-log (optical density $[OD]_{600} = 0.5$) or late ($OD_{600} = 3.2$) stationary phase. Anti-GAPDH was used as loading control.

(I) Schematic of regulation of Rad6 activity in response to stress. Oxidation of Rad6 catalytic cysteine leads to the formation of a Rad6-Uba1 disulfide complex, which inhibits Rad6 activity and controls the levels of K63 ubiquitination in a negative feedback mechanism. Created with BioRender.com.

(J) Immunoblot shows higher levels of K63-linked ubiquitin chain accumulation in Rad6$^{R7A/R11A}$ cells over time. Yeast cells expressing WT Rad6 and a Rad6$^{R7A/R11A}$ mutant generated through CRISPR-Cas9 method were incubated with 0.6 mM H_2O_2 for the respective times.

(K) Immunoblot from cells expressing WT Rad6 and a Rad6$^{R7A/R11A}$ mutant subjected to increasing H_2O_2 concentrations. Rad6$^{R7A/R11A}$ cells show reduced formation of Rad6-Uba1 complex and higher levels of K63 ubiquitin chains. Anti-GAPDH was used as loading control.
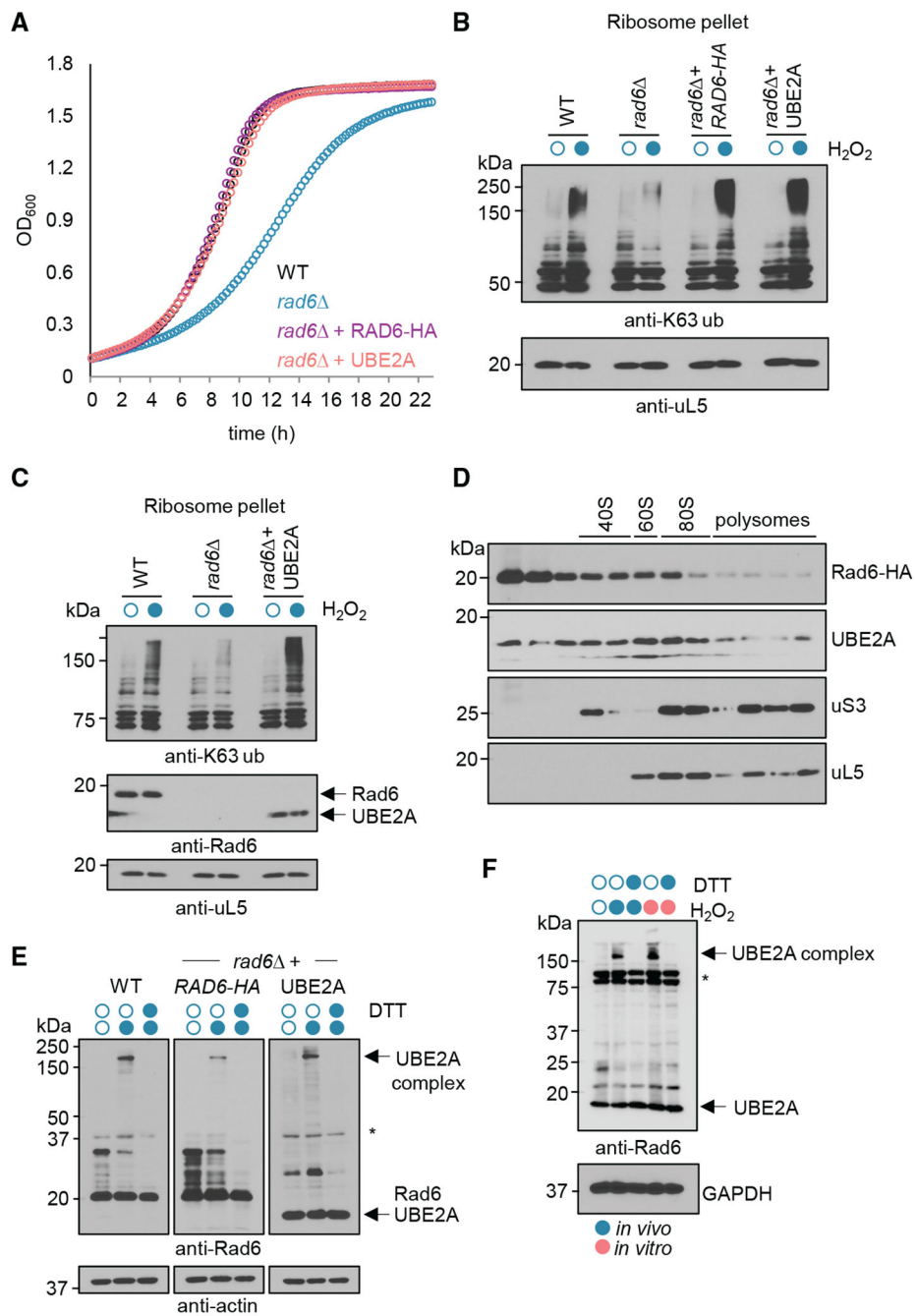
Figure 6. Human UBE2A functionally complements Rad6 in the RTU and is redox regulated

(A and B) Episomal expression of human UBE2A in yeast reverts *rad6* growth defect (A) and ribosomal K63 ubiquitination (B).

(C) Immunoblotting showing that human UBE2A expressed in yeast cells localizes to the ribosome pellet. Anti-Rad6 antibody reacts with both Rad6 and UBE2A. Anti-uL5 was used as loading control.

(D) Immunoblot from yeast cells shows UBE2A presence in the polysome fraction of a sucrose density centrifugation analysis. uS3 and uL5 were used as loading controls.

(E) WT and *rad6* yeast cells expressing UBE2A or Rad6-HA form DTT-reducible (15 mM) disulfides in the cell lysate subjected to 2 mM H_2O_2 incubation for 30 min at RT. Anti-actin was used as loading control. *Anti-Rad6 antibody unspecific band.

(F) UBE2A forms disulfides in HeLa cells after cellular or lysate incubation with 0.5 mM or 2mM H_2O_2, respectively. UBE2A disulfides formed in both conditions are reduced by 15 mM DTT. Anti-GADPH was used as loading control. *Anti-Rad6 antibody unspecific band.
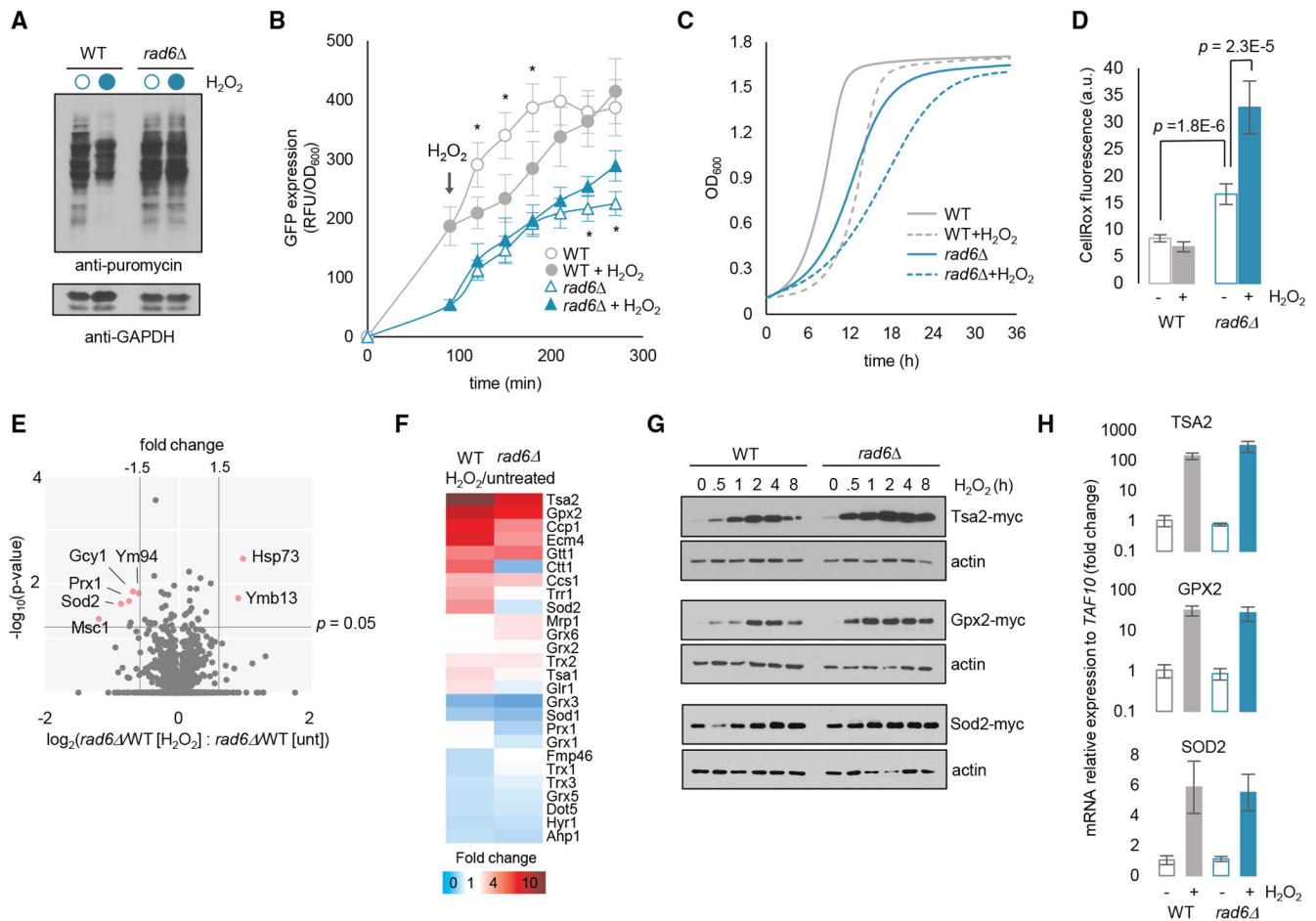
Figure 7. Rad6 supports translation and cellular resistance to stress

(A) Immunoblot of WT and *rad6Δ* cells incubated in the presence or absence of 0.6 mM H_2O_2 for 15 min, following 30 min of puromycin incorporation (0.9 mM) prior to cellular harvesting. Anti-GADPH was used as loading control.

(B) Fluorescence determination of GFP in WT and *rad6Δ* cells. GFP expression was under a Met25 promoter and was induced at time zero by transferring cells to Met-depleted medium. *p < 0.05.

(C) Growth curve of WT and *rad6Δ* strains in the presence (dashed) or absence (solid) of H_2O_2.

(D) Reactive oxygen species (ROS) determination by 2.5 μM CellRox Deep Red fluorometric assay (Thermo Fisher Scientific) from WT and *rad6Δ* cells exposed to 0.6 mM H_2O_2 for 30 min. Fluorescence was captured at 665 nm with excitation at 644 nm. Graph shows mean ± standard deviation for three biological replicates; p values were determined by Student's t test.

(E) Volcano plot of SILAC proteomics ratio from H_2O_2-treated and untreated (unt) WT and *rad6Δ* cells (0.6 mM H_2O_2 for 30 min). Proteins with 1.5× fold change and p <0.05 across three biological replicates are highlighted in the graph.

(F) Heatmap of MS/MS intensity fold change for antioxidant proteins detected in the WT and *rad6Δ* cells.

(G) Immunoblot anti-myc for the expression of the antioxidant proteins Tsa2, Gpx2, and Sod2 in WT and *rad6* cells. Cells were treated with 0.6 mM H_2O_2 for the respective times denoted in the figure. Anti-actin was used as loading control.

(H) Bar graph of qPCR analysis of *TSA2, GPX2*, and *SOD2* transcript levels relative to TAF10 from untreated and H_2O_2-treated WT and *rad6* cells (0.6 mM H_2O_2 for 30 min). Graphs show mean ± standard deviation for three biological replicates.

KEY RESOURCES TABLE

REAGENT or RESOURCE	SOURCE	IDENTIFIER
Antibodies		
Rabbit monoclonal anti-ubiquitin, Lys63-Specific	Millipore Sigma	Cat# 05-1308, Apu3; RRID:AB_1587580
Rabbit polyclonal anti-actin	Cell Signaling	Cat# 4967; RRID:AB_330288
Rabbit polyclonal anti-GAPDH	Abcam	Cat# ab9485; RRID:AB_307275
Mouse monoclonal anti-myc tag	ThermoFisher	Cat# R950-25; RRID:AB_2556560
Rabbit polyclonal anti-myc tag	ThermoFisher	Cat# PA1-981; RRID:AB_325961
Rabbit polyclonal anti-Rad6	Abcam	Cat# ab31917; RRID:AB_777604
Rabbit monoclonal anti-Rps3/uS3	Cell Signaling	Cat# 9538, D50G7; RRID:AB_10622028
Rabbit monoclonal anti-Rpl11/uL5	Cell Signaling	Cat# 18163, D1P5N; RRID:AB_2798794
Rabbit polyclonal anti-HA tag	ThermoFisher	Cat# 71-5500, SG77; RRID:AB_2533988
Rabbit polyclonal anti-Rps20/uS10	ThermoFisher	Cat# PA5-75383; RRID:AB_2719111
Mouse monoclonal anti-ubiquitin	Cell Signaling	Cat# 3936, P4D1; RRID:AB_331292
Mouse monoclonal anti-Ubiquitin	Life Sensors	Cat# VU0101
Mouse monoclonal anti-FLAG M2	Sigma Aldrich	Cat# F3165; RRID:AB_259529
Mouse monoclonal anti-puromycin	Millipore	Cat# MABE343, 12D10; RRID:AB_2566826
Rabbit polyclonal anti-Uba1	Enzo Life Sciences	Cat# BML-PW8395-0025; RRID:AB_2052781
Mouse monoclonal anti-GFP (B-2)	Santa Cruz Biotechnology	Cat# Sc-9996; RRID:AB_627695
Sheep whole anti-mouse IgG HRP-linked	Cytiva	Cat# NA931; RRID:AB_772210
Donkey polyclonal anti-rabbit IgG HRP-linked	Cytiva	Cat# NA934; RRID:AB_772206
Goat anti-Mouse IgG2a heavy chain HRP-linked	Abcam	Cat# ab97245; RRID:AB_10680049
Bacterial and virus strains		
BL21-CodonPlus (DE3)-RIL Competent Cells	Agilent Technologies	Cat#230245
NEB10-beta	New England Biolabs	Cat# C3019
Chemicals, peptides, and recombinant proteins		
MG132 (benzyloxycarbonyl-Leu-Leu-aldehyde)	Sigma-Aldrich	Cat# 474,787; CAS: 133,407-82-6
DL-Dithiothreitol 99.5% (RT)	Sigma-Aldrich	Cat# 43,815; CAS: 3483-12-3
Iodoacetamide	Sigma-Aldrich	Cat# I1149; CAS: 144-48-9
Hydrogen peroxide solution	Sigma-Aldrich	Cat# 216,763; CAS: 7722-84-1
TCEP, Tris(2-carboxyethyl)phosphine hydrochloride	Sigma-Aldrich	Cat# C4706; CAS: 51,805-45-9
L-Buthionine-sulfoximine	Sigma-Aldrich	Cat# B2515; CAS: 83,730-53-4
Adenosine 5′-triphosphate disodium salt hydrate	Sigma-Aldrich	Cat# A2383; CAS: 34,369-07-8
Dimethyl sulfoxide, DMSO	Sigma-Aldrich	Cat# D2650; CAS:67-68-5
Cycloheximide	Sigma-Aldrich	Cat# 01,810; CAS: 66-81-9
3-Methyladenine, autophagy inhibitor 3-MA	Sigma-Aldrich	Cat# M9281; CAS: 5142-23-4
Ubiquitin E1 Inhibitor, PYR-41	Sigma-Aldrich	Cat# 662,105
Creatine phosphate	Sigma-Aldrich	Cat# CAS: 71,519-72-7
Creatine Kinase	Sigma-Aldrich	Cat# 10127566001

REAGENT or RESOURCE	SOURCE	IDENTIFIER
Recombinant Ubiquitin activating enzyme E1 (human) - UBA1	Enzo Life Sciences	Cat# BML-UW9410-0050
Recombinant Ubiquitin-WT	Life Sensors	Cat# si201
Recombinant Ubiquitin-K63R	Life Sensors	Cat# si218
K63-Linked Di-Ubiquitin	Life Sensors	Cat# si6302
Protease Inhibitor Cocktail Set I	Millipore-Sigma	Cat# 539,131
cOmplete™, EDTA-free Protease Inhibitor Cocktail	Roche	Cat# 04693159001
Trypsin/Lys-C Mix	Promega	Cat# V5073
Recombinant eGFP	Novus Biologicals	Cat# NBP2-34923
NBD (4-Chloro-7-nitrobenzofurazan)	Thermo Scientific	Cat# A14165; CAS 10199-89-0
Puromycin	Sigma-Aldrich	Cat# 540,222; CAS 58-58-2
MMS, Methyl metanesulfonate	Sigma-Aldrich	Cat# 129,925
Hydroxyurea, 98%, Alfa Aesar	Fisher Scientific	Cat# AAA1083106
L-Lysine:2HCL unlabeled	Cambridge Isotope Laboratories	Cat# ULM-8766
L-Lysine:2HCL (13C6, 99%; 15N2, 99%)	Cambridge Isotope Laboratories	Cat# CNLM-291-H
Trypsin/Lys-C Mix, Mass Spec Grade	Promega	Cat# V5073
Critical commercial assays		
YeaStar RNA Kit	Zymo Research	Cat# R1002
Q5 Site-Directed Mutagenesis Kit	New England Biolabs (NEB)	Cat# E0552S
FastStart Essential DNA Green Master	Roche Life Science	6402712001
Deposited data		
Structure of Rad6~Ub	Kumar et al., 2015	PDB:4R62
Yeast Rad6	Worthylake et al., 1998	PDB:1AYZ
Yeast 80S ribosome with eEF2	Pellegrino et al., 2018	PDB:6GQ1
Yeast translocating 80S ribosome	Flis et al., 2018	PDB:6GZ5
K63-linked ubiquitinated 80S ribosome	Zhou et al., 2020b	EMD-22198
80S ribosomes from K63R ubiquitin mutant strain	Zhou et al., 2020b	EMD-22196
Ribosomes with conventional 40S beak	This study	EMD-26440
Ribosomes with extended 40S beak	This study	EMD-26441
SILAC RAD6/RAD6^{C88S} redox partner	This study	PXD025726
SILAC protein expression WT/*rad6*	This study	PXD025727
Experimental models: Cell lines		
Human: HeLa	ATCC	Cat# CCL-2
Experimental models: Organisms/strains		
Yeast strains: Refer to Table S3	This study	N/A
Oligonucleotides		
Refer to Table S4	this study	N/A
Recombinant DNA		
Plasmids - Refer to Table S4	this study	N/A
Software and algorithms		

REAGENT or RESOURCE	SOURCE	IDENTIFIER
FlowJo	Becton Dickinson	https://www.flowjo.com
cryoSPARC	Punjani et al., 2017	http://cryosparc
Relion 3.1	Scheres (2012)	https://github.com/3dem/relion
CTFFIND4	Rohou and Grigorieff (2015)	http://grigoriefflab.janelia.org/ctffind4
Pymol	Schrödinger	http://www.pymol.org
Clustal Omega	EMBL-EBI	https://www.ebi.ac.uk/Tools/msa/clustalo/
BioRender	Science Suite Inc.	https://biorender.com/
MaxQuant	Cox and Mann, 2008	www.maxquant.org
Perseus	Tyanova et al., 2016	https://maxquant.net/perseus/